



Universiteit
Leiden
The Netherlands

The tidal disruption event AT2021ehb: evidence of relativistic disk reflection, and rapid evolution of the disk-corona system

Yao, Y.; Lu, W.; Guolo, M.; Pasham, D.R.; Gezari, S.; Gilfanov, M.; ... ; Sollerman, J.

Citation

Yao, Y., Lu, W., Guolo, M., Pasham, D. R., Gezari, S., Gilfanov, M., ... Sollerman, J. (2022). The tidal disruption event AT2021ehb: evidence of relativistic disk reflection, and rapid evolution of the disk-corona system. *The Astrophysical Journal*, 937(1). doi:10.3847/1538-4357/ac898a

Version: Publisher's Version
License: [Creative Commons CC BY 4.0 license](https://creativecommons.org/licenses/by/4.0/)
Downloaded from: <https://hdl.handle.net/1887/3561980>

Note: To cite this publication please use the final published version (if applicable).



The Tidal Disruption Event AT2021ehb: Evidence of Relativistic Disk Reflection, and Rapid Evolution of the Disk–Corona System

Yuhan Yao¹, Wenbin Lu^{2,3}, Muryel Guolo⁴, Dheeraj R. Pasham⁵, Suvi Gezari⁶, Marat Gilfanov^{7,8}, Keith C. Gendreau⁹, Fiona Harrison¹, S. Bradley Cenko⁹, S. R. Kulkarni¹, Jon M. Miller¹⁰, Dominic J. Walton^{11,12}, Javier A. García^{1,13}, Sjoert van Velzen¹⁴, Kate D. Alexander¹⁵, James C. A. Miller-Jones¹⁶, Matt Nicholl¹⁷, Erica Hammerstein¹⁸, Pavel Medvedev⁷, Daniel Stern¹⁹, Vikram Ravi¹, R. Sunyaev^{7,8}, Joshua S. Bloom^{3,20}, Matthew J. Graham¹, Erik C. Kool²¹, Ashish A. Mahabal^{1,22}, Frank J. Masci²³, Josiah Purdum²⁴, Ben Rusholme²³, Yashvi Sharma¹, Roger Smith²⁴, and Jesper Sollerman²¹

¹ Division of Physics, Mathematics and Astronomy, California Institute of Technology, Pasadena, CA 91125, USA; yyao@astro.caltech.edu

² Department of Astrophysical Sciences, 4 Ivy Lane, Princeton University, Princeton, NJ 08544, USA

³ Department of Astronomy, University of California, Berkeley, CA 94720-3411, USA

⁴ Department of Physics and Astronomy, Johns Hopkins University, 3400 N. Charles Street, Baltimore, MD 21218, USA

⁵ Kavli Institute for Astrophysics and Space Research, Massachusetts Institute of Technology, Cambridge, MA 02139, USA

⁶ Space Telescope Science Institute, 3700 San Martin Drive, Baltimore, MD 21218, USA

⁷ Space Research Institute, Russian Academy of Sciences, Profsoyuznaya ul. 84/32, Moscow, 117997, Russia

⁸ Max-Planck-Institut für Astrophysik, Karl-Schwarzschild-Str. 1, D-85741 Garching, Germany

⁹ Astrophysics Science Division, NASA Goddard Space Flight Center, Greenbelt, MD 20771, USA

¹⁰ Department of Astronomy, The University of Michigan, 1085 South University Avenue, Ann Arbor, MI 48103, USA

¹¹ Centre for Astrophysics Research, University of Hertfordshire, College Lane, Hatfield AL10 9AB, UK

¹² Institute of Astronomy, University of Cambridge, Madingley Road, Cambridge CB3 0HA, UK

¹³ Dr. Karl Remeis-Observatory and Erlangen Centre for Astroparticle Physics, Sternwartstr. 7, D-96049 Bamberg, Germany

¹⁴ Leiden Observatory, Leiden University, Postbus 9513, 2300 RA, Leiden, The Netherlands

¹⁵ Center for Interdisciplinary Exploration and Research in Astrophysics (CIERA) and Department of Physics and Astronomy, Northwestern University, Evanston, IL 60208, USA

¹⁶ International Centre for Radio Astronomy Research, Curtin University, GPO Box U1987, Perth, WA 6845, Australia

¹⁷ Birmingham Institute for Gravitational Wave Astronomy and School of Physics and Astronomy, University of Birmingham, Birmingham B15 2TT, UK

¹⁸ Department of Astronomy, University of Maryland, College Park, MD 20742, USA

¹⁹ Jet Propulsion Laboratory, California Institute of Technology, 4800 Oak Grove Drive, Pasadena, CA 91109, USA

²⁰ Lawrence Berkeley National Laboratory, 1 Cyclotron Road, MS 50B-4206, Berkeley, CA 94720, USA

²¹ The Oskar Klein Centre, Department of Astronomy, Stockholm University, AlbaNova, SE-10691, Stockholm, Sweden

²² Center for Data Driven Discovery, California Institute of Technology, Pasadena, CA 91125, USA

²³ IPAC, California Institute of Technology, 1200 E. California Boulevard, Pasadena, CA 91125, USA

²⁴ Caltech Optical Observatories, California Institute of Technology, Pasadena, CA 91125, USA

Received 2022 June 25; revised 2022 August 11; accepted 2022 August 11; published 2022 September 15

Abstract

We present X-ray, UV, optical, and radio observations of the nearby (≈ 78 Mpc) tidal disruption event AT2021ehb/ZTF21aanxhvj during its first 430 days of evolution. AT2021ehb occurs in the nucleus of a galaxy hosting a $\approx 10^7 M_{\odot}$ black hole (M_{BH} inferred from host galaxy scaling relations). High-cadence Swift and Neutron Star Interior Composition Explorer (NICER) monitoring reveals a delayed X-ray brightening. The spectrum first undergoes a gradual soft \rightarrow hard transition and then suddenly turns soft again within 3 days at $\delta t \approx 272$ days during which the X-ray flux drops by a factor of 10. In the joint NICER+NuSTAR observation ($\delta t = 264$ days, harder state), we observe a prominent nonthermal component up to 30 keV and an extremely broad emission line in the iron K band. The bolometric luminosity of AT2021ehb reaches a maximum of $6.0_{-3.8}^{+10.4} \% L_{\text{Edd}}$ when the X-ray spectrum is the hardest. During the dramatic X-ray evolution, no radio emission is detected, the UV/optical luminosity stays relatively constant, and the optical spectra are featureless. We propose the following interpretations: (i) the soft \rightarrow hard transition may be caused by the gradual formation of a magnetically dominated corona; (ii) hard X-ray photons escape from the system along solid angles with low scattering optical depth (\sim a few) whereas the UV/optical emission is likely generated by reprocessing materials with much larger column density—the system is highly aspherical; and (iii) the abrupt X-ray flux drop may be triggered by the thermal–viscous instability in the inner accretion flow, leading to a much thinner disk.

Unified Astronomy Thesaurus concepts: Tidal disruption (1696); X-ray transient sources (1852); Supermassive black holes (1663); Time domain astronomy (2109); High energy astrophysics (739); Accretion (14)

Supporting material: machine-readable table

1. Introduction

A star getting too close to a massive black hole (MBH) can get disrupted by the tidal forces in a tidal disruption event (TDE; see recent review by Gezari 2021). The first observational evidence for TDEs came from the detection of X-ray

flares from the centers of quiescent galaxies during the ROSAT (0.1–2.4 keV) all-sky survey (RASS) in 1990–1991 (Donley et al. 2002). The flares exhibit soft spectra that are consistent with blackbody radiation with temperatures $T_{\text{bb}} \sim 10^6$ K and radii $R_{\text{bb}} \sim \text{few} \times 10^{11}$ cm (Saxton et al. 2020). Since 2020, the Spektrum–Roentgen–Gamma (SRG) mission (Sunyaev et al. 2021), with its sensitive eROSITA telescope (0.2–8 keV; Predehl et al. 2021) and 6 month cadenced all-sky surveys, has become the most prolific discoverer of TDEs in X-rays. The majority of X-ray-selected TDEs are faint in the optical (Sazonov et al. 2021).

In the UV and optical sky, TDEs have been identified as blue nuclear transients in surveys such as the Galaxy Evolution Explorer (Martin et al. 2005), the Panoramic Survey Telescope and Rapid Response System DR1 (Pan-STARRS, PS1; Flewelling et al. 2020; Waters et al. 2020), the Sloan Digital Sky Survey (SDSS, Alam et al. 2015), the All-Sky Automated Survey for SuperNovae (ASAS-SN; Shappee et al. 2014), the Palomar Transient Factory (PTF; Law et al. 2009; Rau et al. 2009), the intermediate PTF (iPTF), the Asteroid Terrestrial-impact Last Alert System (Tonry et al. 2018), and the Zwicky Transient Facility (ZTF; Bellm et al. 2019; Graham et al. 2019). In most cases, the UV/optical spectral energy distribution (SED) can be described by blackbody radiation with larger radii ($R_{\text{bb}} \sim \text{few} \times 10^{14}$ cm) and lower temperatures ($T_{\text{bb}} \sim \text{few} \times 10^4$ K) than those of the X-ray discovered events. The origin of this blackbody component has been attributed to reprocessing of disk emission by an optically thick gas layer (Metzger & Stone 2016; Roth et al. 2016; Lu & Bonnerot 2020), stream self-intersecting shocks formed as a result of general relativistic apsidal precession (Piran et al. 2015; Jiang et al. 2016), or intrinsic thermal emission from the viscously heated accretion disk (Wevers et al. 2021).

Among the UV/optically selected TDEs with simultaneous X-ray observations, about two dozen events have been detected in the X-rays (e.g., Auchettl et al. 2017; Wevers 2020). Their X-ray light curves show a wide range of properties. For example, the X-ray emission of ASASSN-14li lags behind its UV/optical emission by 1 month (Pasham et al. 2017); ASASSN-15oi, AT2018fyk, and AT2019azh exhibit a gradual X-ray brightening long after the UV/optical peak (Gezari et al. 2017; Wevers et al. 2021; Hinkle et al. 2021); AT2019ehz and OGLE16aaa show extreme X-ray flares on a timescale of a few days (van Velzen et al. 2021; Kajava et al. 2020; Shu et al. 2020); and the probable neutrino emitter AT2019dsg has a rapid X-ray decline (Stein et al. 2021). Understanding the coevolution between the X-ray and UV/optical emission may hold the key in deciphering the origin of these two components.

The majority of TDEs are not associated with on-axis relativistic jets (hereafter non-jetted TDEs; Alexander et al. 2020). The sample of jetted TDEs includes four objects: Sw J1644+57 (Bloom et al. 2011; Burrows et al. 2011; Zauderer et al. 2011), Sw J2058+05 (Cenko et al. 2012; Pasham et al. 2015), and Sw J1112–82 (Brown et al. 2015) were discovered by the hard X-ray Burst Alert Telescope on board Swift, whereas AT2022cmc was discovered by ZTF in the optical (Andreoni et al. 2022; Yao et al. 2022a; Pasham et al. 2022). Among them, Sw J1644+57 is the most well studied. Its fast X-ray variability and extremely high isotropic equivalent X-ray luminosity ($\sim 10^{47}$ erg s $^{-1}$) suggest that the early-time X-rays are powered by internal dissipation within a jet. A sudden X-ray flux drop by a factor of $\sim 10^2$ indicates a jet

shut off at rest-frame 370 days after discovery (Zauderer et al. 2013), after which the X-ray emission is consistent with being powered by a forward shock (Eftekhari et al. 2018; Cendes et al. 2021b).

During the outburst of a stellar-mass black hole X-ray binary (XRB), as the mass accretion rate (\dot{M}_{acc}) varies, the X-ray source transitions between distinct spectral states governed by the global evolution of the disk–corona system (Remillard & McClintock 2006). A major question in accretion physics is whether a similar geometry operates in the environment around MBHs. Recent studies of a sample of changing-look active galactic nuclei (CLAGNs) support a scale-invariant nature of black hole accretion flows (McHardy et al. 2006; Walton et al. 2012; Ruan et al. 2019). However, the preexisting gas and dusty torus sometimes complicate interpretation of the observables in CLAGNs (Guolo et al. 2021). On the other hand, the majority of TDEs are hosted by otherwise quiescent galaxies (French et al. 2020). Therefore, TDEs provide ideal laboratories for studying MBH accretion in different regimes (Ulmer 1999; Strubbe & Quataert 2009).

ZTF conducts multiple time-domain surveys using the ZTF mosaic camera (Dekany et al. 2020) on the Palomar Oschin Schmidt 48 inch (P48) telescope. The ZTF team selects TDE candidates by imposing a set of criteria, such as proximity to a galactic nucleus, a lack of pre-flare nuclear activity, and a lack of $g-r$ color change (see detailed descriptions in van Velzen et al. 2019, 2021). The filter is executed by AMPEL (Nordin et al. 2019). We use the Fritz marshal²⁵ to coordinate our follow-up classifications. Thanks to its fast survey speed, ZTF is now reporting ~ 15 TDEs per year (van Velzen et al. 2021; Hammerstein et al. 2022).

AT2021ehb/ZTF21aanxhvj was first detected by the ZTF public 2 day cadence all-sky survey at a brightness of $g_{\text{ZTF}} = 19.10 \pm 0.22$ on 2021 March 1. On 2021 March 3, it was reported to the Transient Name Server (TNS) by the ALeRCE broker (Munoz-Arancibia et al. 2021). On 2021 March 25, AT2021ehb passed our TDE selection filter. Swift observations were triggered while the TDE was still on the rise to peak. On 2021 March 26, we classified AT2021ehb as a TDE based on its nuclear location, persistent blue color, and bright UV emission (Gezari et al. 2021; Yao 2021). Four Swift snapshots from 2021 March 26 to April 2 yielded no X-ray detections. From 2021 April 12 to June 16, AT2021ehb was not observed due to occultation by the Sun. On 2021 June 17, ZTF observations resumed. On 2021 July 1, X-rays were detected with Swift (Yao et al. 2021). Its bright X-ray emission ($\sim 10^{42}$ erg s $^{-1}$) and the subsequent X-ray brightening motivated us to conduct a comprehensive monitoring campaign.

At a spectroscopic redshift of $z = 0.0180$ (see Section 3.1), AT2021ehb is the third closest TDE discovered by optical sky surveys. The previously known lower-redshift events, AT2019qiz (Nicholl et al. 2020) and iPTF16fnl (Blagorodnova et al. 2017), were too faint in the X-ray to be carefully characterized. AT2021ehb, with a peak 0.3–10 keV X-ray flux of 1 mCrab, is the brightest non-jetted TDE in the X-ray sky. We are therefore able to conduct high-cadence monitoring (with Swift and the Neutron Star Interior Composition Explorer, NICER) and obtain high signal-to-noise ratio (S/N) X-ray spectra (with Nuclear Spectroscopic Telescope ARray, NuSTAR; NICER; XMM-Newton; and SRG/eROSITA),

²⁵ <https://github.com/fritz-marshall/fritz>

which allows for the search of spectral line features in the X-ray continuum.

Unlike the X-ray spectra of most other non-jetted TDEs (Saxton et al. 2020; Sazonov et al. 2021), the X-ray spectrum of AT2021ehb drastically evolves over the X-ray observing campaign of ~ 370 days, and at a certain stage, exhibits prominent nonthermal hard emission. Therefore, AT2021ehb is only the second non-jetted TDE, after AT2018fyk (Wevers et al. 2021), which allows us to investigate the rapid evolution between the UV/optical, soft X-ray, and hard X-ray components. Different from the result presented by Wevers et al. (2021), we find that the disk–corona system of AT2021ehb is dissimilar to XRBs.

In this paper, we present an in-depth study of the X-ray, UV, optical, and radio emission of AT2021ehb, using observations obtained from 2021 March 1 to 2022 May 31. We outline the observations in Section 2. We analyze the host galaxy in Section 3, including measurements of the central black hole mass (M_{BH}) and the SED. We study the light curve and spectral evolution of the TDE emission in Section 4. We provide a discussion in Section 5, and conclude in Section 6.

UT time is used throughout the paper. We adopt a standard Λ cold dark matter cosmology with matter density $\Omega_{\text{M}} = 0.3$, dark energy density $\Omega_{\Lambda} = 0.7$, and the Hubble constant $H_0 = 70 \text{ km s}^{-1} \text{ Mpc}^{-1}$, implying a luminosity distance to AT2021ehb of $D_L = 78.2 \text{ Mpc}$. UV and optical magnitudes are reported in the AB system. We use the extinction law from Cardelli et al. (1989), and adopt a Galactic extinction of $E_{B-V, \text{MW}} = 0.123 \text{ mag}$ (Schlafly & Finkbeiner 2011). Uncertainties of X-ray model parameters are reported at the 90% confidence level. Other uncertainties are 68% confidence intervals, and upper limits are reported at 3σ . Coordinates are given in J2000.

2. Observations and Data Reduction

2.1. ZTF Optical Photometry

We obtained ZTF²⁶ forced photometry (Masci et al. 2019) in the g and the r bands using the median position of all ZTF alerts up to MJD 59550 ($\alpha = 03^{\text{h}}07^{\text{m}}47^{\text{s}}.82$, $\delta = +40^{\circ}18'40''.85$). We performed baseline correction following the procedures outlined in Yao et al. (2019).

The peak of the optical light curve probably occurred during Sun occultation and cannot be robustly determined. Therefore, we fitted a five-order polynomial function to the r_{ZTF} -band observations, which suggested that the optical maximum light was around MJD ≈ 59321 . Hereafter we use δt to denote rest-frame days relative to MJD 59321. The Galactic extinction-corrected ZTF light curves are shown in Figure 1. All ZTF photometry is provided in Appendix A.1 (Table 8).

2.2. SEDM and LT Optical Photometry

We obtained additional $ugri$ photometry using the Spectral Energy Distribution Machine (SEDM; Blagorodnova et al. 2018; Rigault et al. 2019) on the robotic Palomar 60 inch telescope (P60; Cenko et al. 2006), and the optical imager on the Liverpool Telescope (LT; Steele et al. 2004). The SEDM photometry was host-subtracted using the automated pipeline FPipe (Fremling et al. 2016). The LT photometry was host-subtracted using SDSS images.

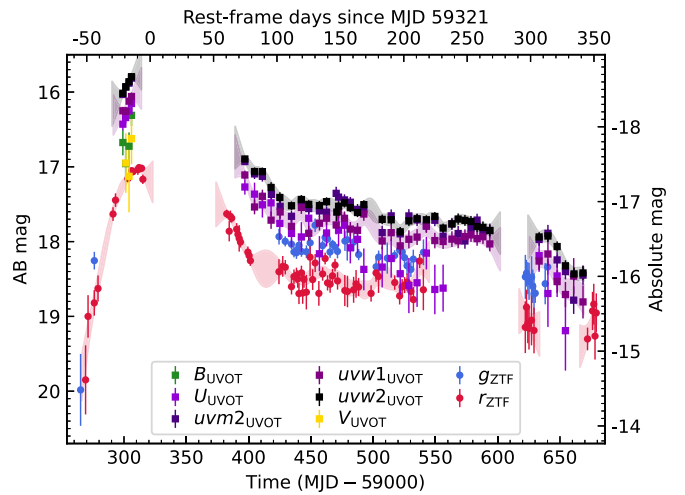


Figure 1. Optical and UV light curves of AT2021ehb. The host contribution has been removed using difference photometry (ZTF, Section 2.1) or subtraction of fluxes estimated from the galaxy SED (Ultra-Violet/Optical Telescope, UVOT; Section 2.4.2). Photometry has only been corrected for Galactic extinction. The transparent lines are simple Gaussian process fits in each filter (see Section 4.1), where the width of the lines represent 1σ model uncertainties. For clarity, we only show the model fits in the r_{ZTF} , $uvw1$, and $uvw2$ bands. Regions where the model uncertainty is greater than 0.3 mag are not shown. The lack of ZTF and UVOT data at $0 \lesssim \delta t \lesssim 50$ days is due to Sun occultation; The lack ZTF data at $220 \lesssim \delta t \lesssim 290$ days and $310 \lesssim \delta t \lesssim 340$ days is due to performance issues with the cooling system for the ZTF Camera (Fremling et al. 2021). The lack of UVOT data at $270 \lesssim \delta t \lesssim 300$ days is due to an issue with one of the Swift reaction wheels (Cenko 2022).

We found a mismatch between the SEDM/LT gr photometry and the ZTF photometry. This is probably a result of different reference images being used. The ZTF difference photometry is more reliable since the reference images were constructed using P48 observations taken in 2018–2019. The reference images of SEDM/LT come from SDSS images (taken in 2005), and long-term variability of the galactic nucleus will render the difference photometry less robust. Therefore, we present the SEDM and LT photometry in Appendix A.1 (Table 8), but exclude them in the following analysis.

2.3. Optical Spectroscopy

We obtained low-resolution optical spectroscopic observations using the Low Resolution Imaging Spectrograph (LRIS; Oke et al. 1995) on the Keck I telescope, the Double Spectrograph (DBSP; Oke & Gunn 1982) on the 200 inch Hale telescope, the integral field unit ($R \approx 100$) spectrograph of SEDM, and the De Veny Spectrograph on the Lowell Discovery Telescope (LDT). We also obtained a medium-resolution spectrum using the Echellette Spectrograph and Imager (ESI; Sheinis et al. 2002) on the Keck II telescope.

Figure 2 shows the low-resolution spectra. The instrumental details and an observing log can be found in Appendix B.

2.4. Swift

AT2021ehb was observed by the X-Ray Telescope (XRT; Burrows et al. 2005) and the Ultra-Violet/Optical Telescope (UVOT; Roming et al. 2005) on board Swift under our GO program 1619088 (as ZTF21aanxhvj; target ID 14217; PI: Gezari) and a series of time-of-opportunity (ToO) requests (PI: Yao). All Swift data were processed with `heasoft` v6.29 c.

²⁶ <https://ztfweb.ipac.caltech.edu/cgi-bin/requestForcedPhotometry.cgi>

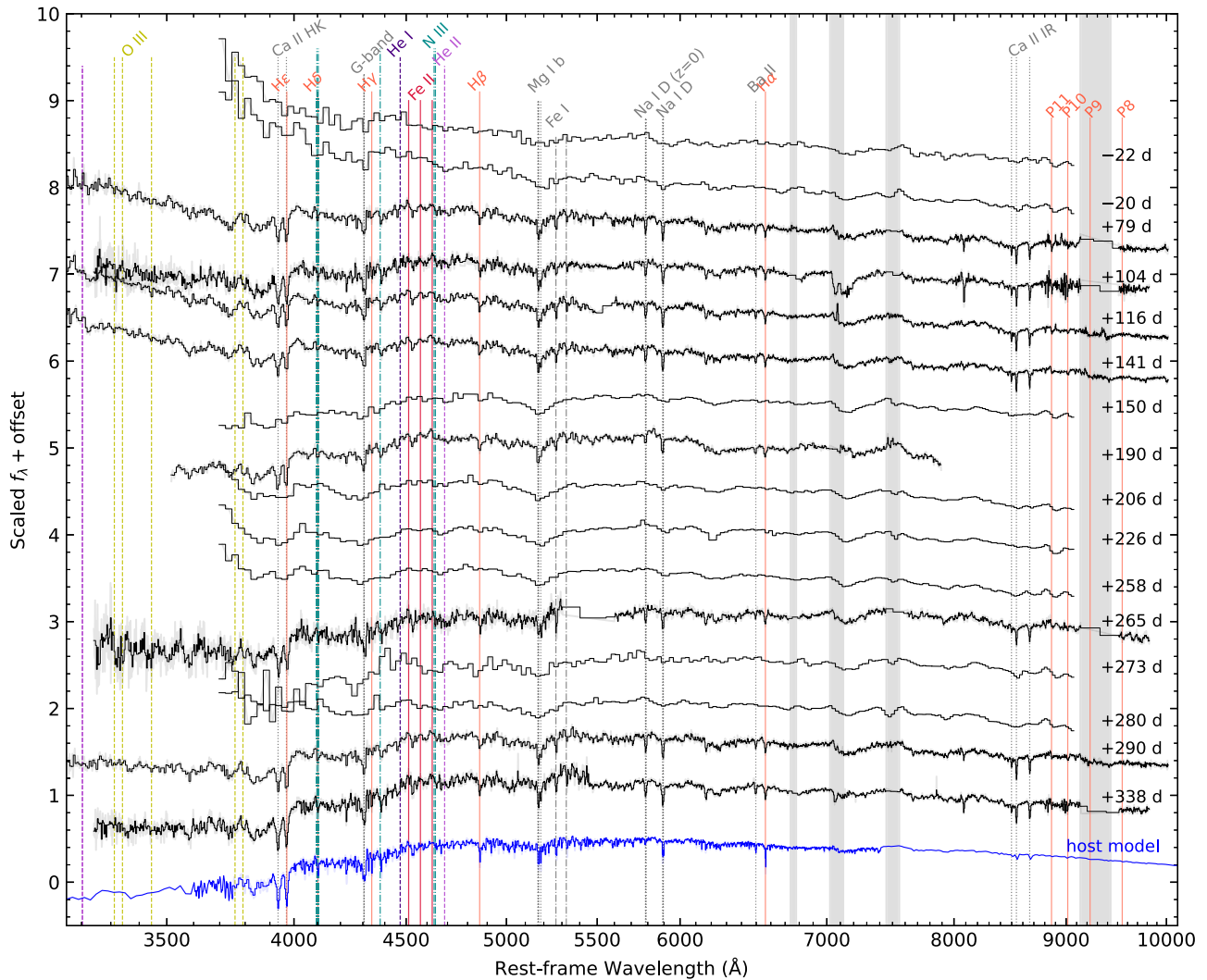


Figure 2. Optical spectroscopic evolution of AT2021ehb. The observed spectra have been corrected for Galactic extinction. The vertical lines mark observed strong host absorption lines and spectral features common in TDEs. The vertical gray bands mark atmospheric telluric features, and strong telluric features have been masked. The best-fit galaxy model is shown at the bottom (see Section 3.2).

2.4.1. XRT

All XRT observations were obtained in the photon-counting mode. First, we ran `ximage` to select snapshots where AT2021ehb was detected above 3σ . For X-ray nondetections, we computed upper limits within a circular region with a radius of $30''$, assuming Poisson statistics. For X-ray detections, to calculate the background-subtracted count rates, we filtered the cleaned event files using a source region with $r_{\text{src}} = 30''$, and eight background regions with $r_{\text{bkg}} = 25''$ evenly spaced at $80''$ from AT2021ehb. A log of XRT observations is given in Appendix A.1 (Table 9).

We generated XRT spectra using an automated online tool²⁷ (Evans et al. 2009). To improve the S/N of each spectrum, we stacked consecutive observations with a similar hardness ratio (HR; see details in Section 4.4.5).

2.4.2. UVOT

The first four UVOT epochs (obsID 14217001–14217005) were conducted with UV+All UV filters. Subsequent observations were conducted with U+All UV filters.

We measured the UVOT photometry using the `uvot-source` tool. We used a circular source region with $r_{\text{src}} = 12''$, and corrected for the enclosed energy within the aperture.²⁸ We measured the background using two nearby circular source-free regions with $r_{\text{bkg}} = 15''$. Following the procedures outlined in van Velzen et al. (2021), we estimated the host galaxy flux in the UVOT bandpass from the population synthesis models (see Section 3.2). The UVOT light curves are presented in Figure 1 and provided in Appendix A.1 (Table 8).

2.5. NICER

AT2021ehb was observed by NICER (Gendreau et al. 2016) under Director’s Discretionary Time (DDT) programs on 2021 March 26, 2021 July 2–7, and from 2021 November 13 to 2022 March 29 (PIs: Yao, Gendreau, Pasham). The NICER data were processed using `nicerdata v9` (2021-08-31_V008c). We ran `nicer12` to obtain the cleaned and screened event files. Background was computed using the `nibackgen3C50` tool (Remillard et al. 2022). Following the screening criteria

²⁷ https://www.swift.ac.uk/user_objects

²⁸ A large aperture is chosen to make sure that all of the flux of the host galaxy is captured.

Table 1
Log of SRG Observations of AT2021ehb

eRASS	MJD	δt (days)	0.3–10 keV flux (10^{-13} erg s $^{-1}$ cm $^{-2}$)
1	58903.59–58904.59	−409.5	<0.25
2	59083.36–59084.70	−232.8	<0.23
3	59253.16–59254.16	−66.1	<0.23
4	59442.45–59443.62	+119.9	$76.8^{+2.5}_{-2.4}$
5	59624.53–59625.70	+298.7	$30.7^{+2.4}_{-2.3}$

Note. Upper limits are computed assuming an absorbed power-law (PL) spectrum with $\Gamma = 2.5$ and $N_{\text{H}} = 9.97 \times 10^{20}$ cm $^{-2}$, and presented at 90% confidence.

suggested by Remillard et al. (2022), we removed “good time intervals” (GTIs) with `hbrcut = 0.05` and `s0cut = 2.0`.

We extracted one spectrum for each obsID, excluding obsIDs with 0.3–1 keV background rate > 0.2 counts s $^{-1}$ or 4–12 keV background rate > 0.1 count s $^{-1}$. Using observations bracketed by the two NuSTAR observations, we also produced two NICER spectra with exposure times of 8.2 ks and 36.6 ks, which we jointly analyzed with the NuSTAR spectra (see Section 4.4.1 and Section 4.4.2).

All NICER spectra were binned using the optimal binning scheme (Kaastra & Bleeker 2016), requiring at least 20 counts per bin. Following the NICER calibration memo,²⁹ we added systematic errors of 1.5% with `grppha`.

2.6. XMM-Newton

We obtained two epochs of follow-up observations with XMM-Newton under our Announcement of Opportunity program (PI: Gezari), on 2021 August 4 (obsID 0882590101) and 2022 January 25 (obsID 0882590901). The observations were taken in full-frame mode with the thin filter using the European Photon Imaging Camera (EPIC; Strüder et al. 2001).

The observation data files were reduced using the XMM-Newton Standard Analysis Software (Gabriel et al. 2004). The raw data files were then processed using the `eproc` task. Since the pn instrument generally has better sensitivity than MOS1 and MOS2, we only analyze the pn data. Following the XMM-Newton data analysis guide, to check for background activity and generate GTIs, we manually inspected the background light curves in the 10–12 keV band. Using the `evselect` task, we only retained patterns that correspond to single and double events (`PATTERN <= 4`).

The source spectra were extracted using a source region of $r_{\text{src}} = 35''$ around the peak of the emission. The background spectra were extracted from an $r_{\text{bkg}} = 108''$ region located in the same CCD. The ancillary response files (ARFs) and response matrix files (RMFs) files were created using the `arfgen` and `rmfgen` tasks, respectively. We grouped the spectra to have at least 25 counts per bin, and limited the over-sampling of the instrumental resolution to a factor of five.

2.7. SRG/eROSITA

The location of AT2021ehb was scanned by eROSITA as part of the planned eight all-sky surveys. Hereafter, eRASS*n*

²⁹ See https://heasarc.gsfc.nasa.gov/docs/nicer/data_analysis/nicer_analysis_tips.html.

Table 2
Radio Observations of AT2021ehb

Date	Δt (days)	ν (GHz)	f_{ν} (μJy)	νL_{ν} (10^{36} erg s $^{-1}$)
2021 Mar 28.85	−18.8	15.0	<16	<1.8
2021 Jul 10.53	83.0	10.0	<16	<1.1
2021 Dec 5.09	228.0	10.0	<16	<1.1
2022 May 6.96	378.1	10.0	<14	<1.1

refers to the *n*th eROSITA all-sky survey.³⁰ During eRASS4, AT2021ehb was independently identified by SRG as a TDE candidate. A log of SRG observations is given in Table 1. We grouped the eRASS4 and eRASS5 spectra to have at least three counts per bin.

2.8. NuSTAR

We obtained NuSTAR (Harrison et al. 2013) observations under a preapproved ToO program (PI: Yao; obsID 80701509002) and a DDT program (PI: Yao; obsID 90801501002). The first epoch was conducted from 2021 November 18.8 to 19.9 with an exposure time of 43.2 ks. The second epoch was conducted from 2022 January 10.4 to 12.1 with an exposure time of 77.5 ks.

To generate the first epoch’s spectra for the two photon-counting detector modules (FPMA and FPMB), source photons were extracted from a circular region with a radius of $r_{\text{src}} = 40''$ centered on the apparent position of the source in both FPMA and FPMB. The background was extracted from an $r_{\text{bkg}} = 80''$ region located on the same detector. For the second epoch, since the source was brighter, we used a larger source radius of $r_{\text{src}} = 70''$, and a smaller background radius of $r_{\text{bkg}} = 65''$.

All spectra were binned first with `ftgrouppha` using the optimal binning scheme developed by Kaastra & Bleeker (2016), and then further binned to have at least 20 counts per bin.

2.9. VLA

We began a monitoring program of AT2021ehb using the Very Large Array (VLA; Perley et al. 2011) under program 20B-377 (PI Alexander). All of the data were analyzed following standard radio continuum image analysis procedures in the Common Astronomy Software Applications (CASA; McMullin et al. 2007). The first three observations used a custom data reduction pipeline (`pwkit`; Williams et al. 2017), while the final observation used the standard NRAO pipeline. AT2021ehb was not detected in any of our observations. All data were imaged using the CASA task `clean`. We computed 3σ upper limits using the `stats` command within the `imtool` package of `pwkit`. The result of the first epoch was reported in Alexander et al. (2021). The full results are presented in Table 2.

In Figure 3, we compare the radio luminosity of AT2021ehb with other UV- and optically selected TDEs. We note that AT2021ehb looks to be significantly (by more than an order of magnitude) radio-underluminous compared to previously observed non-jetted TDEs at similar times post-peak. It has

³⁰ Here, *n* runs from 1 to 8. As of April 2022, eRASS1–eRASS4 have been completed, and 38% (sky area) of eRASS5 has been completed.

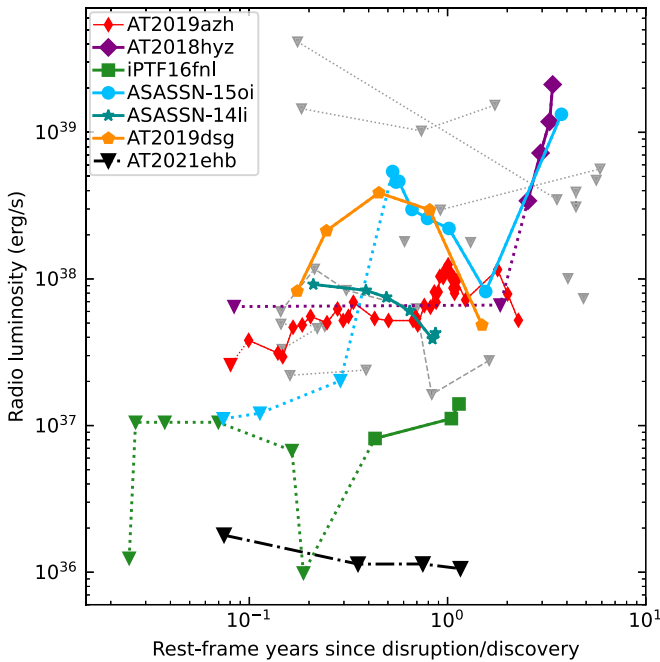


Figure 3. Radio upper limits for AT2021ehb in the context of other UV- and optically discovered TDEs with radio data, including ASASSN-14li (Alexander et al. 2016), ASASSN-15oi (Horesh et al. 2021a), iPTF16fnl (Horesh et al. 2021b), AT2018fyz (Wevers et al. 2019a, 2021), AT2018hzy (Cendes et al. 2022), AT2019azh (Goodwin et al. 2022; Sfaradi et al. 2022), AT2019dsg (Cendes et al. 2021a), and upper limits listed in Table 2 of Alexander et al. (2020).

the deepest limits on any TDE radio emission at >150 days post-discovery.

3. Host Galaxy Analysis

Figure 4 shows the pre-TDE optical image centered on AT2021ehb, using data from PS1. The host galaxy appears to be close to edge-on.

3.1. Velocity Dispersion and Black Hole Mass

The host galaxy absorption lines are prominent in the optical spectra (see Figure 2). Using our medium-resolution ($R = 5350$) spectrum taken with Keck II/ESI, we measured the line centers of strong absorption lines, and determined the redshift to be $z = 0.0180$.

Following previous TDE work (Wevers et al. 2017, 2019b; French et al. 2020), we measured the stellar velocity dispersion by fitting the normalized ESI spectrum (see pre-processing procedures in Appendix B) with the penalized pixel-fitting (pPXF) software (Cappellari & Emsellem 2004; Cappellari 2017). pPXF fits the absorption line spectrum by convolving a library of stellar spectra with Gauss-Hermite functions. We adopted the ELODIE v3.1 high-resolution ($R = 42,000$) template library (Prugniel & Soubiran 2001; Prugniel et al. 2007).

To robustly measure the velocity dispersion and the associated uncertainties, we performed 1000 Monte Carlo (MC) simulations, following the approach adopted by Wevers et al. (2017). In each fitting routine, we masked wavelength ranges of common galaxy emission lines and hydrogen Balmer lines. The derived velocity dispersion is $\sigma = 92.9^{+5.3}_{-5.2}$ km s $^{-1}$ at the 95% confidence interval.

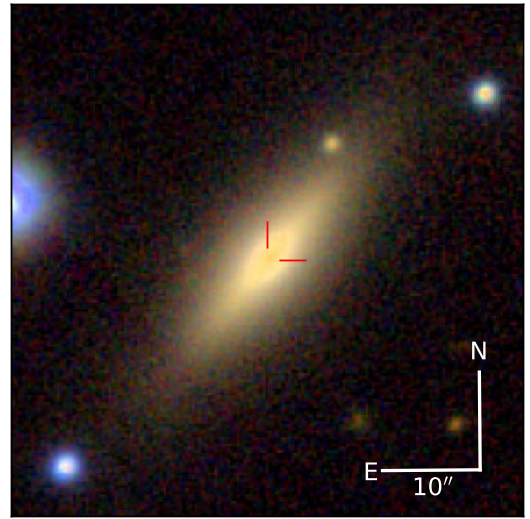


Figure 4. PS1 RGB false-color $g/i/z$ image centered on AT2021ehb. North is up and east to the left. A $10''$ scale bar is included.

Table 3
Observed Photometry of the Host Galaxy

Catalog	Band	λ_{eff} (nm)	Magnitude
SDSS	u	355	17.748 ± 0.019
SDSS	g	467	15.814 ± 0.003
SDSS	r	616	14.901 ± 0.002
SDSS	i	747	14.443 ± 0.003
SDSS	z	892	14.094 ± 0.004
2MASS	J	1232	13.951 ± 0.025
2MASS	H	1642	13.676 ± 0.034
2MASS	K_s	2157	13.893 ± 0.043
AllWISE	W1	3346	14.816 ± 0.024
AllWISE	W2	4595	15.535 ± 0.022
AllWISE	W3	11553	16.756 ± 0.229

According to the $M_{\text{BH}}-\sigma$ relation (Kormendy & Ho 2013), the measured σ corresponds to a black hole mass of $\log(M_{\text{BH}}/M_{\odot}) = 7.03 \pm 0.15(\text{stat}) \pm 0.29(\text{sys})$, where 0.29 is the intrinsic scatter of the $M_{\text{BH}}-\sigma$ relation. If adopting the Ferrarese & Ford (2005) $M_{\text{BH}}-\sigma$ relation, then $\log(M_{\text{BH}}/M_{\odot}) = 6.60 \pm 0.20(\text{stat}) \pm 0.34(\text{sys})$. Hereafter we adopt the result from the Kormendy & Ho (2013) relation because it includes more low-mass galaxies.

We note that although the Kormendy & Ho (2013) relation was originally calibrated mainly at an M_{BH} regime that is too massive to produce a TDE, recent studies show that the same relation holds in the dwarf galaxy regime (Baldassare et al. 2020).

3.2. Host SED Model

We constructed the pre-TDE host galaxy SED using photometry from SDSS, the Two Micron All-Sky Survey (2MASS; Skrutskie et al. 2006), and the AllWISE catalog (Cutri et al. 2014). The photometry of the host is shown in Table 3.

Our SED fitting approach is similar to that described in van Velzen et al. (2021). We used the flexible stellar population synthesis (FSPS) code (Conroy et al. 2009), and adopted a delayed exponentially declining star formation history (SFH) characterized by the e -folding timescale τ_{SFH} . The

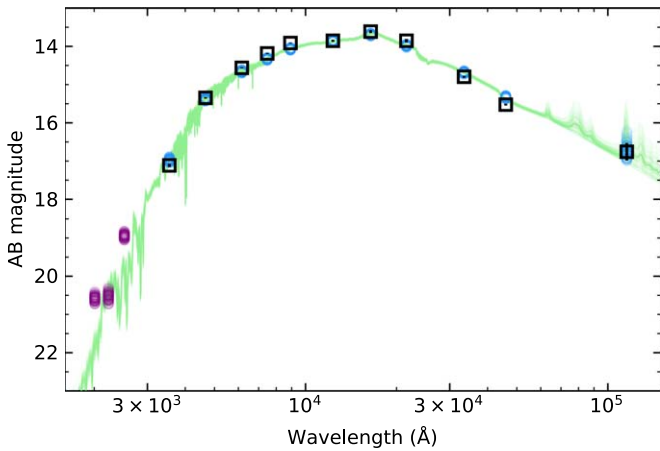


Figure 5. Host galaxy SED of AT2021ehb. The open squares are the Galactic extinction-corrected host photometry (see Table 3). The green lines are samples from the posterior distribution of host galaxy SED models. The open circles are the synthetic host galaxy magnitudes in the observed bands (shown in blue) and in the UV filters of Swift/UVOT (shown in purple).

Prospector package (Johnson et al. 2021) was utilized to run a Markov Chain Monte Carlo sampler (Foreman-Mackey et al. 2013). We show the best-fit model prediction of the host galaxy optical spectrum at the bottom of Figure 2.

From the marginalized posterior probability functions, we obtain the total galaxy stellar mass $\log(M_*/M_\odot) = 10.18_{-0.02}^{+0.01}$, the metallicity, $\log Z = -0.57 \pm 0.04$, $\tau_{\text{SFH}} = 0.19_{-0.07}^{+0.18}$ Gyr, the population age, $t_{\text{age}} = 12.1_{-0.6}^{+0.3}$ Gyr, and negligible host reddening ($E_{B-V,\text{host}} = 0.01 \pm 0.01$ mag). The best-fit SED model is shown in Figure 5.

Following Gezari (2021), we use the $M_{\text{BH}}-M_*$ relation from Greene et al. (2020) to obtain a black hole mass of $\log(M_{\text{BH}}/M_\odot) = 7.14 \pm (0.10+0.79)$, where 0.79 is the intrinsic scatter of the scaling relation. This is consistent with the M_{BH} inferred from the $M_{\text{BH}}-\sigma$ relation (Section 3.1).

To summarize, the host galaxy of AT2021ehb has a total stellar mass of $M_* \approx 10^{10.18} M_\odot$ and a BH mass of $M_{\text{BH}} \approx 10^{7.03} M_\odot$. The measured black hole mass is on the high end of the population of optically selected TDEs (French et al. 2020; Nicholl et al. 2022), and is too massive to disrupt a white dwarf (Rosswog et al. 2009).

4. Analysis of the TDE Emission

4.1. UV/optical Photometric Analysis

To capture the general trend of AT2021ehb’s UV/optical photometric evolution, we fit the data in each filter using a combination of five-order polynomial functions and Gaussian process smoothing, following procedures described in Appendix B.4 of Yao et al. (2020). The model fits in r_{ZTF} , $uvw1$, and $uvw2$ are shown as semitransparent lines in Figure 1.

We then define a set of “good epochs” close in time to actual multiband measurements, and fit a Planck function to each set of fluxes to determine the effective temperature T_{bb} , photospheric radius R_{bb} , and blackbody luminosity of the UV/optical emitting component L_{bb} . We initially assume $E_{B-V,\text{host}} = 0$ mag, and then repeat the procedure under different assumptions about the host reddening. We find that the fitting residual monotonically increases as $E_{B-V,\text{host}}$ increases from 0 mag to 0.2 mag, suggesting negligible host

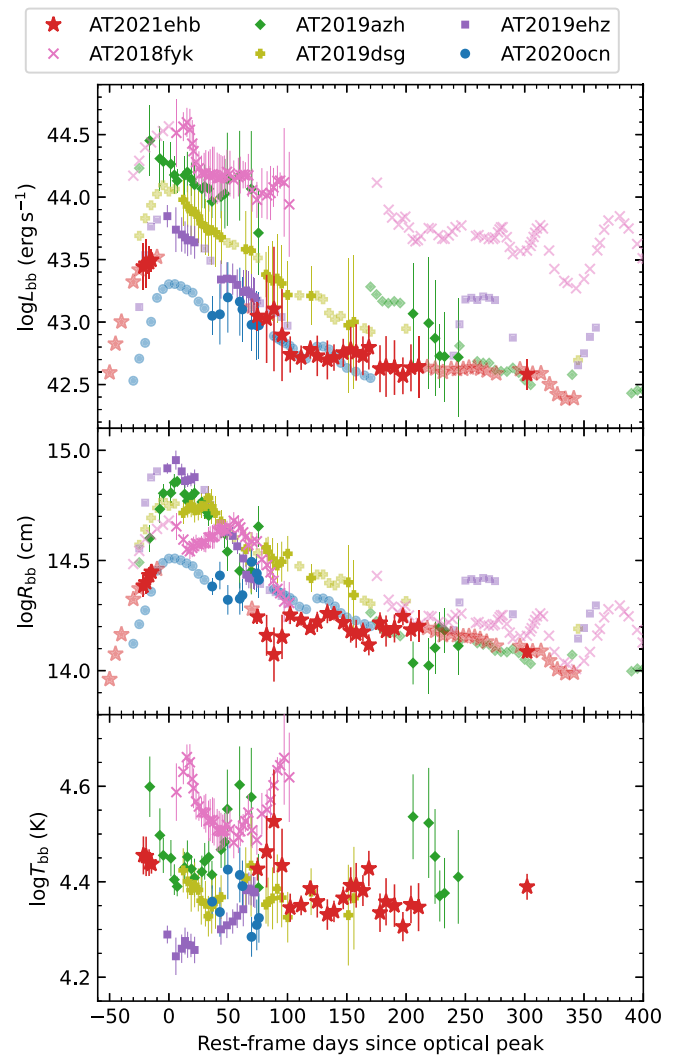


Figure 6. Evolution of the UV/optical blackbody properties of AT2021ehb compared with a sample of recent X-ray bright TDEs in the literature, including AT2018fyk (Wevers et al. 2019a, 2021), AT2019dsg (Stein et al. 2021), AT2019azh (Hinkle et al. 2021), AT2020ocn, and AT2019ehz (van Velzen et al. 2021). The results of “good epochs” (see definition in the text) are shown in high-opacity colors, whereas results of “ok epochs” are shown in semitransparent.

reddening. Therefore, for the remainder of this discussion, we assume $E_{B-V,\text{host}} = 0$ mag.

We also define a set of “ok epochs” where we only have photometric observations in the optical (or only in the UV). Due to a lack of wavelength coverage, T_{bb} and R_{bb} can not be simultaneously constrained. As such we fix the T_{bb} values by interpolating the T_{bb} evolution of “good epochs,” and fit for R_{bb} values of “ok epochs.”

The physical parameters derived from the blackbody fits are presented in Table 10 (Appendix A.2) and shown in Figure 6, where they are compared with a sample of recent TDEs with multiple X-ray detections. We have measured the blackbody parameters of other TDEs using the same procedures described above.

While the temperature of AT2021ehb ($T_{\text{bb}} \sim 2.5 \times 10^4$ K) is typical among optical and X-ray bright TDEs, its peak radius ($R_{\text{bb}} \sim 3 \times 10^{14}$ cm) and luminosity ($L_{\text{bb}} \sim 3 \times 10^{43}$ erg s $^{-1}$) are at the low end of the distributions. We note that in the ZTF-I sample of 30 TDEs (Hammerstein et al. 2022), only two

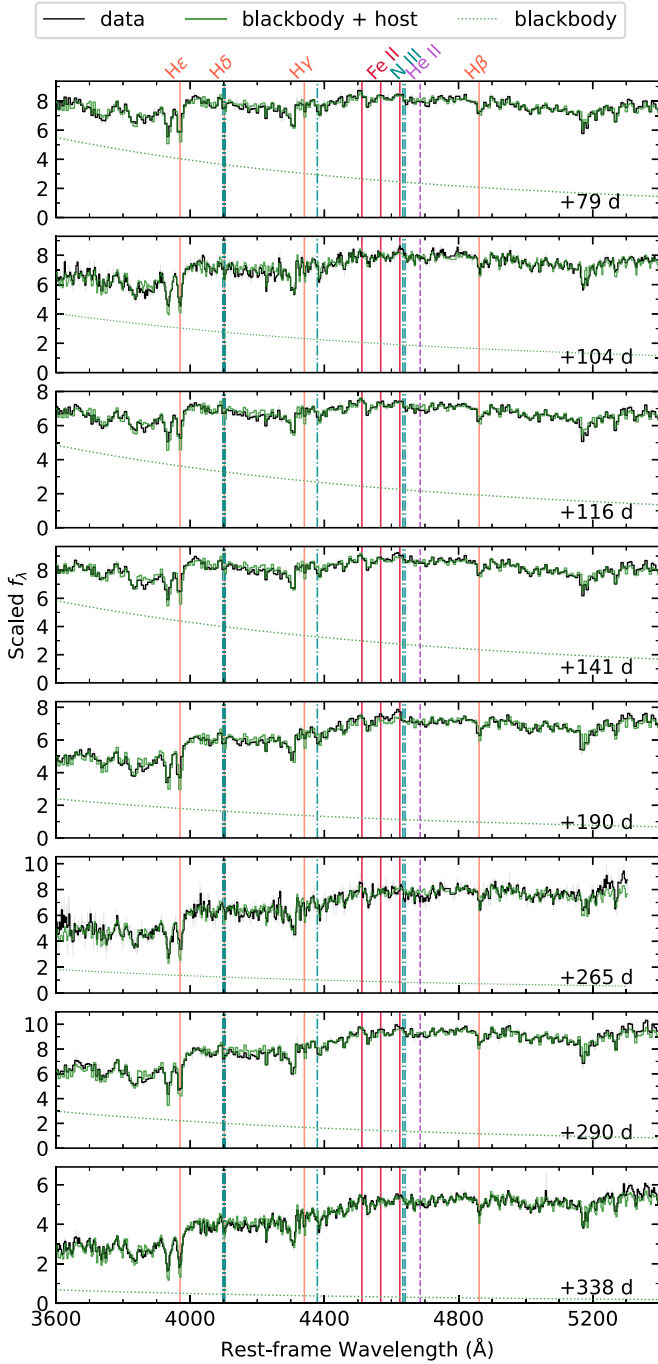


Figure 7. Long-slit optical spectra of AT2021ehb taken at eight different epochs. The spectrum ($f_{\lambda,\text{obs}}$) is plotted in black. The blackbody continuum ($A_1 f_{\lambda, \text{BB}}$; dotted lines) plus host galaxy spectrum ($A_2 f_{\lambda, \text{host}}$) is plotted in green. No spectral features commonly seen in optically selected TDEs are observed in AT2021ehb.

objects (AT2020ocn and AT2019wey) have peak radii smaller than that of AT2021ehb (see the discussion in Section 5.4.1).

4.2. Optical Spectral Analysis

Figure 2 shows that no broad line is evident in the optical spectra of AT2021ehb. To search for weak spectral features from the TDE, we fit the Galactic extinction-corrected long-slit spectra in rest-frame 3600–5400 Å using a combination of blackbody emission and host galaxy contribution: $f_{\lambda,\text{obs}} = A_1 f_{\lambda, \text{BB}} + A_2 f_{\lambda, \text{host}}$. Here $f_{\lambda, \text{BB}} = \pi B_{\lambda}(T_{\text{bb}})(R_{\text{bb}}^2/D_L^2)$,

where T_{bb} and R_{bb} are obtained by linearly interpolating the blackbody parameters derived in Section 4.1 at the relevant δt . $f_{\lambda, \text{host}}$ is the predicted host galaxy spectrum obtained in Section 3.2 convolved with the instrumental broadening σ_{inst} (see Appendix B). A_1 and A_2 are constants added to account for unknown factors, including the varying amount of host galaxy flux falling within the slit (which depends on the slit width, slit orientation, seeing conditions, and target acquisition), uncertainties in the absolute flux calibration, and the adopted blackbody parameters. We note that $f_{\lambda, \text{host}}$ is the predicted spectrum for the whole galaxy, and therefore might not be a perfect description of the bulge spectrum.

The fitting results are shown in Figure 7. We mark locations of emission lines commonly seen in TDEs, including Balmer lines, He II, the Bowen fluorescence lines of N III and O III, as well as low-ionization Fe II lines (Blanchard et al. 2017; Wevers et al. 2019a; van Velzen et al. 2021). The observed spectra of AT2021ehb can be well described by a blackbody continuum (dotted lines) plus host galaxy contribution. The spectra at $\delta t > 170$ days are mostly from the host, and therefore it is not very surprising that no discernible TDE lines were detected. However, at $\delta t < 170$ days, the blackbody component contributes 25%–80% of the total flux. As such, it is surprising that no prominent lines from the TDE itself can be identified. We further discuss this result in Section 5.4.1.

4.3. X-Ray Light-curve Analysis

The middle panel of Figure 8 shows the XRT and NICER (all binned by obsID) light curves. The lower panel of Figure 8 shows the evolution of the hardness ratio, defined as $\text{HR} \equiv (H - S)/(H + S)$, where H is the number of net counts in the hard band, and S is the number of net counts in the soft band, for XRT, we take 1–10 keV as the hard band, while for NICER, we take 1–4 keV.

X-rays were not detected at $\delta t < 0$. Pre-peak X-ray upper limits are provided by Swift/XRT ($< 10^{40.9} \text{ erg s}^{-1}$; Table 9) and SRG/eROSITA ($< 10^{40.2} \text{ erg s}^{-1}$; Table 1).

X-rays were first detected by XRT at $\delta t = 73.9$ days. The exact time of the X-ray onset cannot be accurately constrained. The count rate initially exhibited strong variability from $\delta t = 73.9$ days to $\delta t = 82.3$ days, and then gradually increased out to $\delta t = 250$ days. At the same time, the HR gradually increased. From $\delta t = 250$ days to $\delta t = 271$ days, both the X-ray flux and the hardness stayed at the maximum values.

From $\delta t = 271.0$ days to $\delta t = 273.7$ days, the NICER net count rate suddenly decreased by a factor of 10 (Yao et al. 2022b). At the same time, the HR significantly decreased. After an X-ray plateau of ≈ 50 days, the XRT net count rate further decreased drastically by a factor of six (from $\delta t = 320.9$ days to $\delta t = 327.2$ days).

4.4. X-Ray Spectral Analysis

In this subsection, we first present a joint spectral analysis of contemporaneous data sets obtained from NICER and NuSTAR, including the first epoch in 2021 November 18–19 (Section 4.4.1) and the second epoch in 2022 January 10–12 (Section 4.4.2). These observations are of high S/N and cover a wide energy range. As such, the fitting results can guide us to choose appropriate spectral models to fit spectra with lower S/Ns. We then perform analysis on data sets obtained by single telescopes, including XMM-Newton (Section 4.4.3), SRG

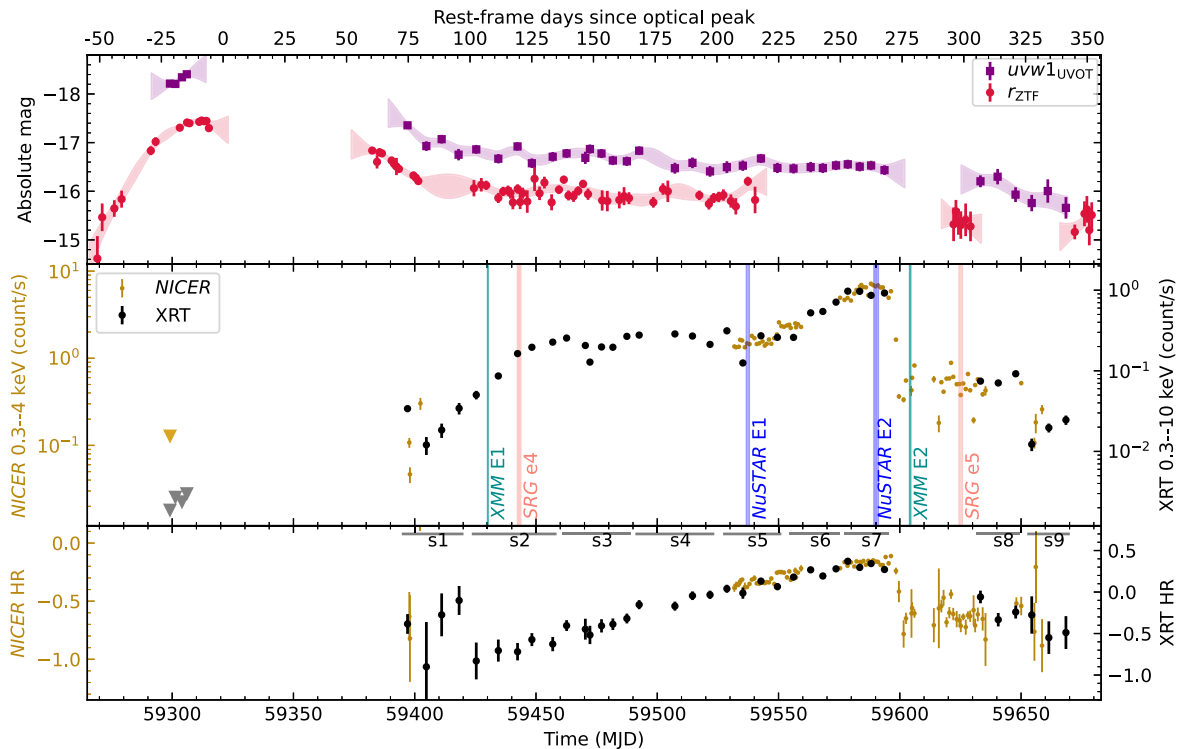


Figure 8. Upper: UV ($uvw1_{UVOT}$) and optical (r_{ZTF}) light curves of AT2021ehb. Middle: XRT and NICER X-ray net count rates of AT2021ehb. Epochs of XMM-Newton, SRG, and NuSTAR observations are marked by the vertical lines. Lower: XRT and NICER hardness ratio (HR) evolution of AT2021ehb.

(Section 4.4.4), Swift/XRT (Section 4.4.5), and NICER (Section 4.4.6).

All spectral fitting was performed with `xspec` (v12.12, Arnaud 1996). We used the `vern` cross sections (Verner et al. 1996). The `wilm` abundances (Wilms et al. 2000) were adopted in Sections 4.4.1 and 4.4.2, whereas the Anders & Grevesse (1989) abundances were adopted in Sections 4.4.3, 4.4.4, 4.4.5, and 4.4.6.

4.4.1. NICER+NuSTAR First Epoch, 2021 November

We chose energy ranges where the source spectrum dominates over the background. For NICER we used 0.3–4 keV. For NuSTAR/FPMA we used 3–23 keV, and for FPMB we used 3–20 keV.³¹ All data were fitted using χ^2 -statistics.

For all spectral models described below, we included the Galactic absorption using the `tbabs` model (Wilms et al. 2000), with the hydrogen-equivalent column density N_H fixed at $9.97 \times 10^{20} \text{ cm}^{-2}$ (HI4PI Collaboration et al. 2016). We shifted the TDE emission using the convolution model `zshift`, with the redshift z fixed at 0.018. We included possible absorption intrinsic to the source using the `ztbabs` model. We also included a calibration coefficient (`constant`; Madsen et al. 2017) between FPMA, FPMB, and NICER, with $C_{FPMA} \equiv 1$. This term also accounts for the differences in the mean flux between NuSTAR and NICER that results from intrinsic source variability.

First, we fitted the spectrum with a power law (PL), and obtained a photon index of $\Gamma \approx 2.7$. The fit is unacceptable, with the reduced χ^2 being $\chi_r^2 = 3.44$ for 144 degrees of freedom

(dof). The residuals are most significant between 0.3 and 2 keV, suggesting the existence of a (thermal) soft component. Therefore, we changed the PL to `simpl*thermal_model`. Here `simpl` is a Comptonization model that generates the PL component via Compton scattering of a fraction (f_{sc}) of input seed photons (Steiner et al. 2009). The flag R_{up} was set to 1 to only include up-scattering. We experimented with three different thermal models: a blackbody (`bbody`), a multicolor disk (MCD; `diskbb`; Mitsuda et al. 1984), and a single-temperature thermal plasma (`bremss`; Kellogg et al. 1975), resulting in $\chi_r^2 = 1.33$, 1.15, and 1.35 (for dof = 142), respectively. The fit statistics favors an MCD.

The best-fit result with an MCD, defined as model (1a), is shown in Figure 9. We present the best-fit parameters in Table 4. Here, T_{in} is the inner disk temperature, and $R_{in}^* \equiv R_{in} \sqrt{\cos i}$ is the apparent inner disk radius times the square root of $\cos i$, where i is the system inclination. R_{in}^* is inferred from the normalization parameter of `diskbb`. Model (1a) gives a good fit with $\chi_r^2 = 163/142 = 1.15$.

4.4.2. NICER+NuSTAR Second Epoch, 2022 January

We chose energy ranges where the source spectrum dominates over the background. For NICER, we used 0.3–7.0 keV; for NuSTAR FPMA and FPMB, we used 3–30 keV. All data were fitted using χ^2 -statistics. Unlike in Section 4.4.1, here we use `tbfeo` to model the Galactic absorption. Compared with `tbabs`, `tbfeo` allows the O and Fe abundances (A_O , A_{Fe}) to be free.

We adopted a continuum model of `simpl*diskbb`, defined as (2a). The result, with $\chi_r^2 = 2.04$, is shown in Figure 10 and the upper-left panel of Figure 11. The best-fit parameters are given in Table 5. The residual plot clearly

³¹ In this NuSTAR observation, FPMB is more affected by a nearby bright source.

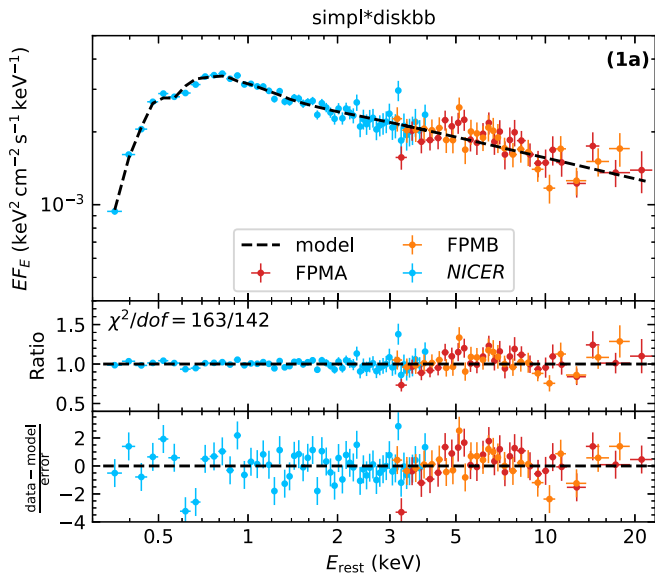


Figure 9. The spectrum of the first joint NICER and NuSTAR observations (2021 November). See Table 4 for best-fit parameters. NuSTAR/FPMB and NICER data have been divided by C_{FPMB} and C_{NICER} , respectively. The data have been rebinned for visual clarity.

Table 4

Modeling of the First Joint NICER and NuSTAR Observations, $\delta t = 212$ Days

Component	Parameter	(1a)
constant	C_{FPMB}	$1.03^{+0.06}_{-0.05}$
	C_{NICER}	$0.85^{+0.06}_{-0.05}$
ztbabs	N_{H} (10^{20}cm^{-2})	<0.75
simpl	Γ	2.29 ± 0.05
	f_{sc}	$0.35^{+0.02}_{-0.03}$
diskbb	T_{in} (eV)	164^{+6}_{-9}
	R_{in}^* (10^4km)	$25.5^{+4.4}_{-2.0}$
...	χ^2/dof	$163.17/142 = 1.15$

indicates the existence of unmodeled spectral features and a significant offset between NuSTAR and NICER at 6–7 keV.

First, we study whether this offset is brought about by a cross-calibration difference between NICER and NuSTAR. To this end, we replaced `constant` with `crabcorr` (Ludlam et al. 2022), which multiplies the spectrum by a PL of $C \cdot E^{-\Delta\Gamma}$. When $\Delta\Gamma=0$, `crabcorr` is equivalent to `constant`. We fixed $\Delta\Gamma_{\text{FPMA}} = \Delta\Gamma_{\text{FPMB}} = 0$, and allow $\Delta\Gamma_{\text{NICER}}$ to be free. The best-fit model gives $\Delta\Gamma_{\text{NICER}} = -0.128^{+0.014}_{-0.023}$, which is too large compared with the value of $\Delta\Gamma_{\text{NICER}} \approx -0.06$ found by Ludlam et al. (2022). Therefore, we conclude that a difference in the cross-calibration slope is likely not the primary reason for the 6–7 keV offset.

Next, we investigate whether this offset is caused by imperfect NICER calibration at 2–3 keV. NICER effective area changes rapidly in the 2–3 keV band. Calibration issues in that range may cause the model to overestimate the data at 2–3 keV, and to badly underestimate it above 3 keV. As a test, we performed the fit omitting the 2–3 keV region in the NICER data. However, the best-fit result still leaves a significant offset between NICER and NuSTAR at 6–7 keV, similar to that shown in Figure 10.

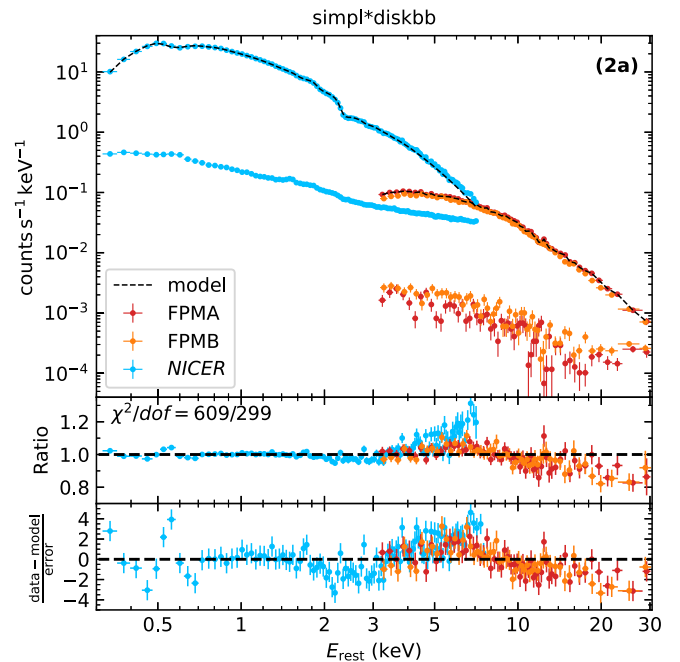


Figure 10. The spectrum of the second joint NICER and NuSTAR observations (2022 January). This figure highlights the flux levels of the source and background spectra.

We are left to conclude that the offset is likely caused by either an underestimate of NICER background at the high-energy end or systematic uncertainties in NICER calibration that is not well characterized. This conjecture is based on the fact that NICER uses X-ray concentrators optics, and its 3–7 keV background is >10 times brighter than that of NuSTAR (Figure 10). On the other hand, NuSTAR adopts X-ray focusing optics, which enables more robust background estimation using regions close to the object of interest.

In the following, we attempted to improve the fit by three approaches: adding a Gaussian line, adding reflection emission features, and adding absorption features.

Modeling with a Gaussian Line Profile—The result with adding a Gaussian line component is shown in the upper-right panel of Figure 11. This model, defined as (2b), provides a much better fit compared with (2a). The best-fit parameters (Table 5) give a very broad emission profile with a central energy at $E_{\text{line}} \sim 5 \text{keV}$ and a line width of $\sigma_{\text{line}} \sim 2 \text{keV}$. If the 3–7 keV spectral feature indeed comes from an emission line, its central energy is different from the emission line at $E_{\text{line}} \sim 8 \text{keV}$ that has been found in the jetted TDE Sw J1644+57, which has been interpreted as highly ionized iron $K\alpha$ emission blueshifted by $\sim 0.15c$ (Kara et al. 2016; Thomsen et al. 2019). Instead, what is shown here indicates the possible existence of a relativistically broadened iron line (either redshifted or with a more distorted red wing).

Modeling with Disk Reflection—In this method, we fit the data using a combination of MCD and relativistic reflection from an accretion disk.

We utilize the self-consistent `relxill` model to describe the direct PL component and the reflection part (García et al. 2014; Dauser et al. 2014). In `relxill`, we fixed the outer disk radius (R_{out}) at a fiducial value of $400 R_{\text{g}}$, since it has little effect on the X-ray spectrum. The redshift parameter in `relxill` was fixed at 0 since the host redshift was already included by the `zshifft` model. To reduce the complexity of

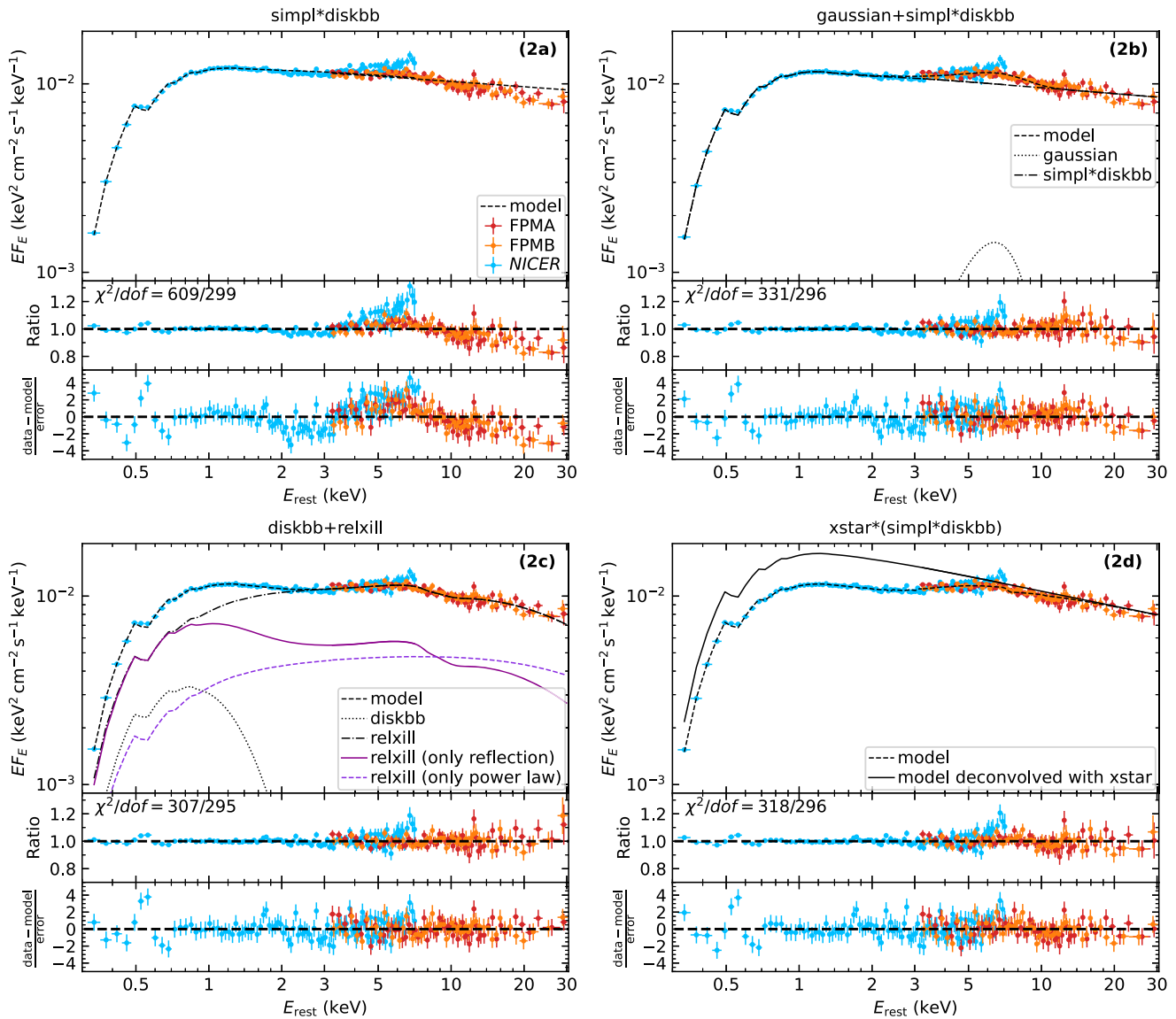


Figure 11. The spectrum of the second joint NICER and NuSTAR observations (2022 January). See Table 5 for best-fit parameters. NuSTAR/FPMB and NICER data have been divided by C_{FPMB} and C_{NICER} , respectively. The data have been rebinned for visual clarity. In the lower-left panel, we also show the reflection contribution and the direct PL contribution individually from `relxill`. In the lower-right panel, we also show the best-fit model (2d) deconvolved with the `xstar` component.

this model, we froze the reflection fraction R_{F} (ratio of the reflected to primary emission; Dauser et al. 2016) at 1. The inner and outer emissivity index q were fixed at 3 throughout the accretion disk, making R_{break} obsolete. We assume the inner disk radius is at the innermost stable circular orbit (ISCO), i.e., $R_{\text{in}} = R_{\text{ISCO}}$. Other parameters in `relxill` include the PL index of the incident spectrum Γ , the cutoff energy of the PL E_{cut} , the black hole spin a , the inclination i , the ionization of the accretion disk ξ , the iron abundance of the accretion disk A_{Fe} , and the normalization parameter Norm_{rel} . We first fit the data allowing a to be free, finding that the fit is not sensitive to a . Therefore, we performed the fit with a fixed at zero.

The best-fit model, hereafter (2c), gives $\chi^2/\text{dof} = 306.65/296 = 1.04$ and is shown in the lower-left panel of Figure 11. The best-fit model parameters are given in Table 5. In Figure 12, the solid black line shows the best-fit model; Modifications of the best-fit model are shown as dotted (if a is changed from 0 to 0.998), dashed (if i is changed from 43.4° to 70°), and dashed-dotted (if $\log \xi$ is changed from 4.09 to 3.50)

lines. The shape and width of the extremely broad iron emission are mainly determined by the high disk ionization state and the moderate inclination. We note that the best-fit ionization of $\xi \sim 10^4 \text{ erg cm s}^{-1}$ is greater than the typical values observed in Seyfert 1 active galactic nuclei (AGNs; Walton et al. 2013; Ezhikode et al. 2020).

Modeling with Absorbers—In this method, we attempt to improve the fit by adding absorption features. First, we added partial covering of a neutral absorber using the `pcfabs` model. In `pcfabs`, a fraction f_{cover} of the X-ray source is seen through a neutral absorber with hydrogen-equivalent column density N_{H} , while the rest is assumed to be observed directly. The best-fit model gives $\chi^2/\text{dof} = 386/297 = 1.30$. If we add a new free parameter (redshift of the neutral absorber) by replacing `pcfabs` with `zpcfabs`, χ^2/dof becomes $370/296 = 1.25$. However, both models leave 5–8 keV flux excess in the residual.

Therefore, we next allow the absorber to be partially ionized by replacing `zpcfabs` with a photoionized absorber. This is also motivated by the fact that a good fit to the Chandra LETG

Table 5
Modeling of the Second Joint NICER and NuSTAR Observations, $\delta t = 264$ Days

Component	Parameter	(2a)	(2b)	(2c)	(2d)	
constant	C_{FPMB}	1.03	1.03 ± 0.01	1.03 ± 0.01	1.03 ± 0.01	
	C_{NICER}	0.98	1.02 ± 0.01	1.02 ± 0.01	1.03 ± 0.01	
tbfeo	A_{O}	1.40	$1.48^{+0.11}_{-0.08}$	1.26 ± 0.13	$1.45^{+0.10}_{-0.07}$	
	A_{Fe}	1.80	$2.07^{+0.63}_{-0.64}$	$1.99^{+0.61}_{-0.62}$	$2.37^{+0.50}_{-0.39}$	
ztbabs	$N_{\text{H}} (10^{20} \text{ cm}^{-2})$	0.00	< 0.12	0.70 ± 0.28	< 0.01	
diskbb	$T_{\text{in}} (\text{eV})$	187	198^{+8}_{-6}	257 ± 8	180^{+7}_{-2}	
	$R_{\text{in}}^* (10^4 \text{ km})$	31.7	$28.4^{+1.2}_{-1.7}$	$10.5^{+1.0}_{-0.9}$	47.3 ± 2.8	
simpl	Γ	2.09	2.11 ± 0.01	...	2.26 ± 0.01	
	f_{sc}	0.52	$0.49^{+0.02}_{-0.03}$...	0.61 ± 0.01	
Gaussian	$E_{\text{line}} (\text{keV})$...	$4.92^{+0.36}_{-0.71}$	
	$\sigma_{\text{line}} (\text{keV})$...	$2.18^{+0.50}_{-0.32}$	
	Norm ($10^{-4} \text{ ph cm}^{-2} \text{ s}^{-1}$)	...	$2.52^{+1.01}_{-0.51}$	
relxill	$q_1 = q_2$	3 (frozen)	...	
	a	0 (frozen)	...	
	i ($^\circ$)	$43.4^{+8.5}_{-9.6}$...	
	$R_{\text{in}} (R_{\text{ISCO}})$	1 (frozen)	...	
	$R_{\text{out}} (R_g)$	400 (frozen)	...	
	Γ	1.86 ± 0.02	...	
	$\log \xi (\text{erg cm s}^{-1})$	$4.09^{+0.20}_{-0.12}$...	
	A_{Fe}	$1.86^{+1.46}_{-0.63}$...	
	$E_{\text{cut}} (\text{keV})$	$54.0^{+13.4}_{-9.5}$...	
	R_{F}	1 (frozen)	...	
	Norm (10^{-5})	$6.1^{+0.40}_{-0.40}$...	
	xstar	$N_{\text{H}} (10^{23} \text{ cm}^{-2})$	$2.22^{+0.49}_{-0.86}$
		$\log \xi (\text{erg cm s}^{-1})$	$1.51^{+0.34}_{-0.32}$
f_{cover}		0.31 ± 0.02	
Redshift		0 (frozen)	
...	χ^2/dof	$609.43/299 = 2.04$	$330.72/296 = 1.12$	$306.64/295 = 1.04$	$318.23/296 = 1.08$	

Note. Parameter uncertainties of model (2a) cannot be calculated since $\chi_r^2 > 2$.

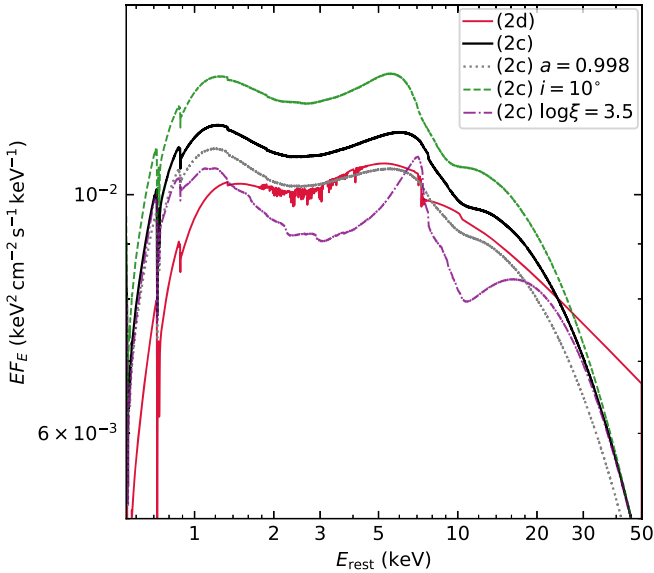


Figure 12. Best-fit incident model spectra of (2c) and (2d), as well as modifications of (2c) if one parameter is changed.

observation conducted on 2021 November 29 was found with such a model by Miller et al. (2022a). This fit utilized the `zxcipcf` model (Reeves et al. 2008), which is a grid of photoionization models computed by the `XSTAR` code (Kallman & Bautista 2001). However, Reynolds et al. (2012) noted that `zxcipcf` only has a very coarse sampling in

ionization space, and so in this work, we use an updated `XSTAR` grid that is suitable for use with AGNs (computed in Walton et al. 2020). This grid assumes an ionizing continuum of $\Gamma = 2$ and a velocity broadening of 100 km s^{-1} , and allows the ionization parameter, column density, absorber redshift, and both the oxygen and iron abundances to be varied as free parameters (although for simplicity we assume these abundances are solar). Fitting the data with the redshift of the absorber fixed at zero yields $\chi^2/\text{dof} = 318.2/296 = 1.08$. If the redshift is allowed to be free, we have $\chi^2/\text{dof} = 317.7/295 = 1.08$. Since χ^2 only reduces by 0.5 for 1 dof, the redshift parameter cannot be well constrained by our data. Therefore, we name the model with the absorber redshift fixed at zero as (2d), and show it in the lower-right panel of Figure 11. The model parameters are given in Table 5. In Figure 12, the solid crimson line shows a high-resolution version of model (2d).

Model Comparison and Comments—Between (2b) and (2c), we consider (2c) to be superior since (i) its χ^2 is smaller by 24 for only 1 dof, and (ii) it adopts a physically motivated model instead of a mathematical function.

To compare (2c) and (2d), we use the Bayesian information criterion (BIC) to assess the goodness of fit. Here

$$\text{BIC} = k \cdot \ln(N) - 2 \ln L \quad (1)$$

$$= k \cdot \ln(N) + \chi^2 + \text{constant} \quad (2)$$

where k is the number of free parameters, N is the number of spectral bins, and \mathcal{L} is the maximum of the likelihood function.

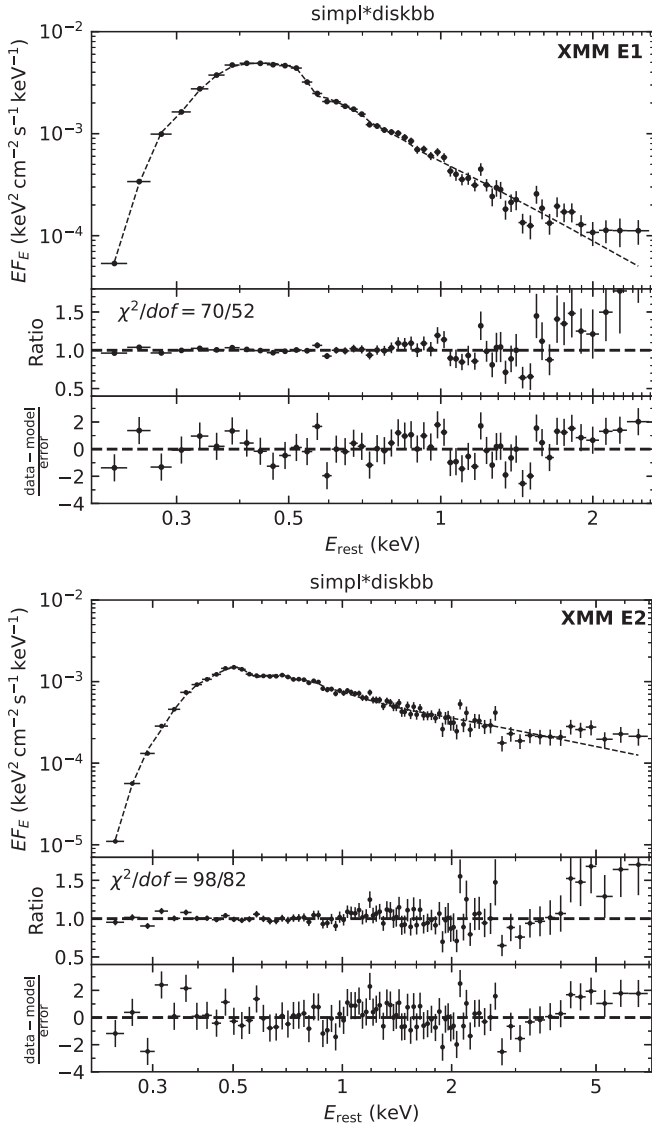


Figure 13. The XMM-Newton spectra. The data have been rebinned for visual clarity. The dashed lines show the best-fit models. See Table 6 for the best-fit parameters.

Models with lower BIC values are favored. According to Raftery (1995), a BIC difference between 2 and 6 is positive, a difference between 6 and 10 is strong, and a difference greater than 10 is very strong. Since $\text{BIC}(2c) - \text{BIC}(2d) = -5.9$, model (2c) is slightly favored over (2d). The energy range over which model (2c) performs better than (2d) is $\sim 8\text{--}12$ keV. This is because absorption by ionized iron adds a relatively sharp flux decrease at ~ 7 keV, while the blue wing of the iron emission in *relxill* is smoother (see the lower-right panel of Figure 11).

We note that the residual below 0.7 keV is strong in all model fits, and is likely caused by underestimated NICER calibration uncertainties at the lowest energies.

4.4.3. XMM-Newton Analysis

We chose energy ranges where the source spectrum dominates over the background. For XMM E1, this is 0.2–2.6 keV, while for XMM E2 this is 0.2–7.0 keV. All data

Table 6
Modeling of Two XMM-Newton Observations

Component	Parameter	XMM E1	XMM E2
ztbabs	N_{H} (10^{20} cm $^{-2}$)	$1.09^{+0.99}_{-0.45}$	<1.22
diskbb	T_{in} (eV)	68^{+1}_{-4}	125 ± 8
	R_{in}^* (10^4 km)	511^{+144}_{-75}	39^{+10}_{-6}
simpl	Γ	$>4.57^{\text{a}}$	2.92 ± 0.15
	f_{sc}	$0.13^{+0.03}_{-0.01}$	0.16 ± 0.03
...	χ^2/dof	$70.26/52 = 1.35$	$97.49/82 = 1.19$

^a Upper limit of Γ is at 5.

were fitted using χ^2 -statistics. Following Sections 4.4.1 and 4.4.2, all models described below have been multiplied by *tbabs*ztbabs*zashift* to include Galactic absorption, host absorption, and host redshift.

Although the XMM E1 spectrum is very soft, a single MCD results in a poor fit and leaves a large residual above 1 keV, suggesting the existence of a nonthermal component. A continuum model of *simpl*diskbb* gives a much better fit with $\chi_r^2 = 1.35$. The best-fit model is shown in the upper panel of Figure 13. The XMM E2 spectrum is much harder than that from XMM E1. Fitting with *simpl*diskbb* gives a good fit with $\chi_r^2 = 1.19$ (see Figure 13, lower panel).

We note that although the χ_r^2 of our best-fit XMM-Newton models are acceptable, there seems to be some systematic residuals. For example, eight consecutive bins of positive residuals are seen in the 1.7–2.6 keV XMM E1 data. A possible explanation is that there exist spectral features created by absorbing materials in the TDE system, such as the blueshifted absorption lines reported in the TDE ASASSN-14li (Miller 2015; Kara et al. 2018). Seven consecutive bins of positive residuals are seen in the 4.0–7.0 keV XMM E2 data. This might indicate the existence of disk reflection features, such as an iron emission line. We note that 2–4 days after our second XMM-Newton epoch, XMM-Newton/EPIC observations obtained under another program also reveals the existence of interesting features in the iron *K* band (Miller et al. 2022b). More detailed modeling of the XMM-Newton spectra is beyond the scope of this paper, and is encouraged in future work.

4.4.4. SRG/eROSITA Analysis

We chose energy ranges where the source spectrum dominates over the background. For eRASS4 this range is 0.2–3 keV, while for eRASS5 this range is 0.2–2 keV. All data were fitted with the *C*-statistic (Cash 1979).

Following Section 4.4.1 and Section 4.4.3, we fitted the SRG/eROSITA spectra with *tbabs*ztbabs*zashift*simpl*diskbb*. For the eRASS5 spectrum, since the source is only above background at 0.2–2 keV, the PL index cannot be constrained from the SRG/eROSITA spectrum alone. Therefore, we fixed Γ at the best-fit value of the XMM E2 spectrum (Table 6, $\Gamma = 2.92$), and allowed other parameters to be free. This choice is based on the fact that the XMM E2 and eRASS5 observations appear to show the same properties on the light curve and hardness evolution diagrams (Figure 8).

The fitting results are shown in Figure 14. The best-fit parameters are shown in Table 7.

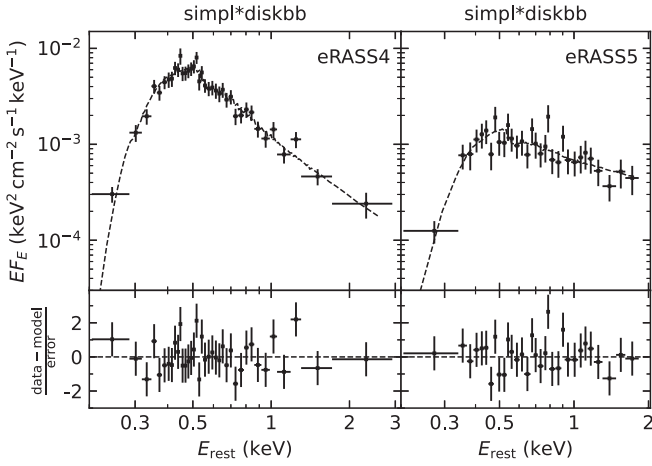

Figure 14. SRG/eROSITA spectra of AT2021ehb.

Table 7
 Modeling of Two SRG/eROSITA Observations

Component	Parameter	eRASS4	eRASS5
ztbabs	N_{H} (10^{20} cm^{-2})	$0.21^{+2.19}_{-0.20}$	<3.41
diskbb	T_{in} (eV)	89^{+7}_{-13}	96^{+32}_{-22}
	R_{in}^* (10^4 km)	210^{+179}_{-38}	73^{+243}_{-21}
simpl	Γ	$4.15^{+0.82}_{-0.73}$	2.92 (frozen)
...	f_{sc}	$0.14^{+0.12}_{-0.08}$	$0.21^{+0.06}_{-0.09}$
...	$cstat/dof$	126.43/140	76.45/85

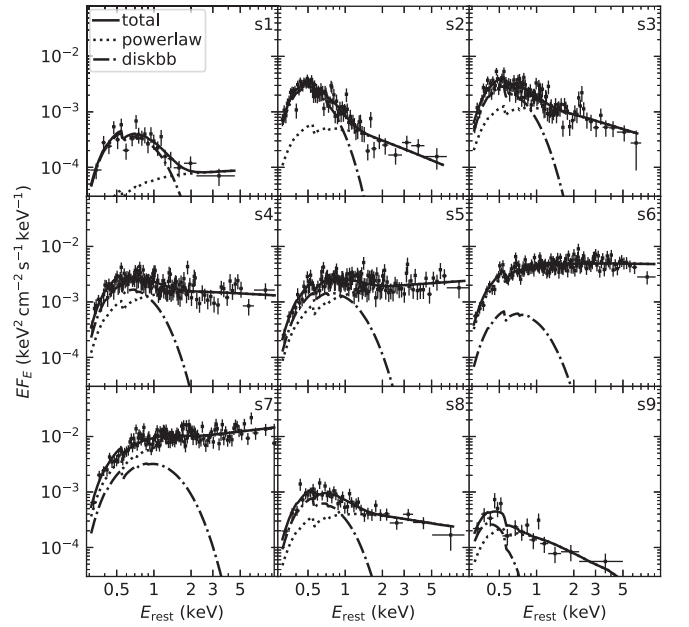
4.4.5. XRT Analysis

The temporal coverage of each time-averaged XRT spectrum (generated in Section 2.4.1) is shown as “s1,” “s2,” ..., “s9” in the lower panel of Figure 8. We fitted the 0.3–10 keV spectra using a simple model of `tbabs*zashift*(diskbb+powerlaw)`. We did not include the `ztbabs` component, as host galaxy absorption was found to be negligible or much smaller than the Galactic absorption in all previous spectral analyses (see Tables 4, 5, 6, and 1). The adopted continuum model does not give realistic model parameters. For example, the disk radii will be underestimated when the source spectrum is hard (see a detailed discussion in Steiner et al. 2009). The main goal of this fitting is to compute the multiplicative factor to convert the 0.3–10 keV XRT net count rate to X-ray fluxes, including (i) the observed 0.3–10 keV flux $f_{\text{X}}(0.3\text{--}10 \text{ keV})$, (ii) the Galactic absorption corrected 0.3–10 keV flux $f_{\text{X},0}(0.3\text{--}10 \text{ keV})$, (iii) the Galactic absorption corrected 0.5–10 keV flux $f_{\text{X},0}(0.5\text{--}10 \text{ keV})$, and (iv) the Galactic absorption corrected flux density at the rest-frame energies of 0.5 keV and 2 keV (i.e., $f_{\nu}(0.5 \text{ keV})$ and $f_{\nu}(2 \text{ keV})$). All data were fitted using *C*-statistics.

The best-fit models are shown in Figure 15. Scaling factors to convert 0.3–10 keV net count rate to X-ray fluxes can be computed using values provided in Table 11 (Appendix A.2). The observed isotropic equivalent 0.3–10 keV X-ray luminosity, L_{X} , is shown in the upper panel of Figure 16. Note that for the initial four XRT nondetections, we assume a spectral shape similar to “s1.”

4.4.6. NICER Analysis

We started with the obsID-binned NICER spectra generated in Section 2.5. We only performed spectral fitting on obsIDs


Figure 15. XRT time-averaged spectra of AT2021ehb. See the lower panel of Figure 8 for the time span of each spectrum.

with more than 500 total net counts in 0.3–4 keV. Following Section 4.4.5, we fitted a `tbabs*zashift*(diskbb+powerlaw)` model to the 0.3–4 keV spectra and inferred f_{X} from the best-fit models. All data were fitted using χ^2 -statistics. The best-fit models provided a χ^2_{ν} close to 1 in most cases. The L_{X} evolution inferred from NICER spectral fitting is also shown in the upper panel of Figure 16.

4.5. Spectral Indices α_{OX} and α_{OSX}

To assist comparison with TDEs from the literature, we computed the UV to X-ray spectral index α_{OX} (Tananbaum et al. 1979; Ruan et al. 2019; Wevers et al. 2021) and α_{OSX} (Gezari 2021), which are commonly used in AGN and TDE literature to characterize the ratio of UV to X-ray fluxes.³² Here

$$\alpha_{\text{OX}} \equiv \frac{\log[L_{\nu}(2500 \text{ \AA})/L_{\nu}(2 \text{ keV})]}{\log[\nu(2500 \text{ \AA})/\nu(2 \text{ keV})]}, \quad (3)$$

$$\alpha_{\text{OSX}} \equiv \frac{\log[L_{\nu}(2500 \text{ \AA})/L_{\nu}(0.5 \text{ keV})]}{\log[\nu(2500 \text{ \AA})/\nu(0.5 \text{ keV})]}, \quad (4)$$

where L_{ν} is the luminosity at a certain frequency (corrected for N_{H} and $E_{B-V,MW}$). We use the `Swiftuvw1` host-subtracted luminosities (rest-frame effective wavelength at 2459 \AA for $T_{\text{eff}} = 3 \times 10^4 \text{ K}$) as a proxy for $L_{\nu}(2500 \text{ \AA})$. We measure $f_{\nu}(0.5 \text{ keV})$ and $f_{\nu}(2 \text{ keV})$ by converting the XRT net count rates to flux densities using the scaling factors derived in Section 4.4.5. We note that $f_{\nu}(2 \text{ keV})$ mainly traces the evolution of the nonthermal X-ray component, while $f_{\nu}(0.5 \text{ keV})$ traces both the thermal and nonthermal components. The results are shown in the lower panel of Figure 16.

Based on Figure 16, we divide the evolution of AT2021ehb into five phases. In phase A ($\delta t \lesssim 0$ days), the UV/optical luminosity brightens, while X-rays are not detected

³² Note that some papers use these indices with a minus sign in front of our definitions.

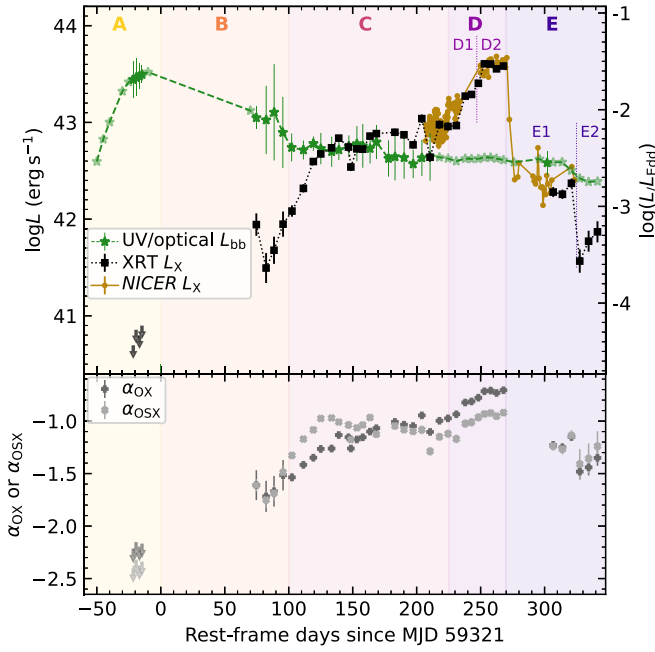


Figure 16. Upper: blackbody luminosity of the UV/optical emission (L_{bb} ; Section 4.1) compared with the observed isotropic equivalent 0.3–10 keV X-ray luminosity (L_{X}) from XRT (Section 4.4.5) and NICER (Section 4.4.6). Lower: the 2500 Å to X-ray spectral slope measured by Swift observations (Equation (3), (4)).

($<10^{40.9}$ erg s $^{-1}$). In phase B ($0 \lesssim \delta t \lesssim 100$ days), the UV/optical luminosity declines, and X-rays emerge. Entering into phase C ($100 \lesssim \delta t \lesssim 225$ days), the X-ray spectrum gradually hardens, while the UV/optical luminosity stays relatively flat. In phase D ($225 \lesssim \delta t \lesssim 270$ days), the X-ray further brightens two times (indicated by D1 and D2), and the UV/optical plateau persists. In phase E, the X-ray luminosity drops two times (indicated by E1 and E2), while the UV/optical luminosity only slightly declines. Interestingly, the dramatic X-ray evolution in phase D+E does not have much effect on the UV/optical luminosity. Typical SEDs in each phase are shown in Figure 17.

4.6. Bolometric Luminosity L_{bol}

To calculate the bolometric luminosity L_{bol} at the epochs of the Swift observations, we assume that the bulk of the radiation is between 10,000 Å and 10 keV. We estimate that when the X-ray spectrum is the hardest (i.e., model 2c), the 0.3–10 keV flux still constitutes 72% of the 0.3–100 keV flux. Therefore, this assumption at most underestimates $\log L_{\text{bol}}$ by 0.14 dex.

We compute the 10,000 Å to 10 keV luminosity by adding the luminosities in three energy ranges (see a demonstration in Figure 18).

From 10,000 Å to 2500 Å, we integrate below the blackbody model fitted to the UV/optical photometry (Section 4.1).

From 2500 Å to 0.5 keV, we assume that the TDE spectrum is continuous and can be approximated by a PL of $f_{\nu} \propto \nu^{\alpha_{\text{OSX}}}$. Hence, the luminosity is

$$L = \int_{\nu_1}^{\nu_2} L_{\nu} d\nu \approx \int_{\nu_1}^{\nu_2} \frac{L_{\nu}(\nu_1)}{\nu_1^{\alpha_{\text{OSX}}}} \nu^{\alpha_{\text{OSX}}} d\nu \quad (5)$$

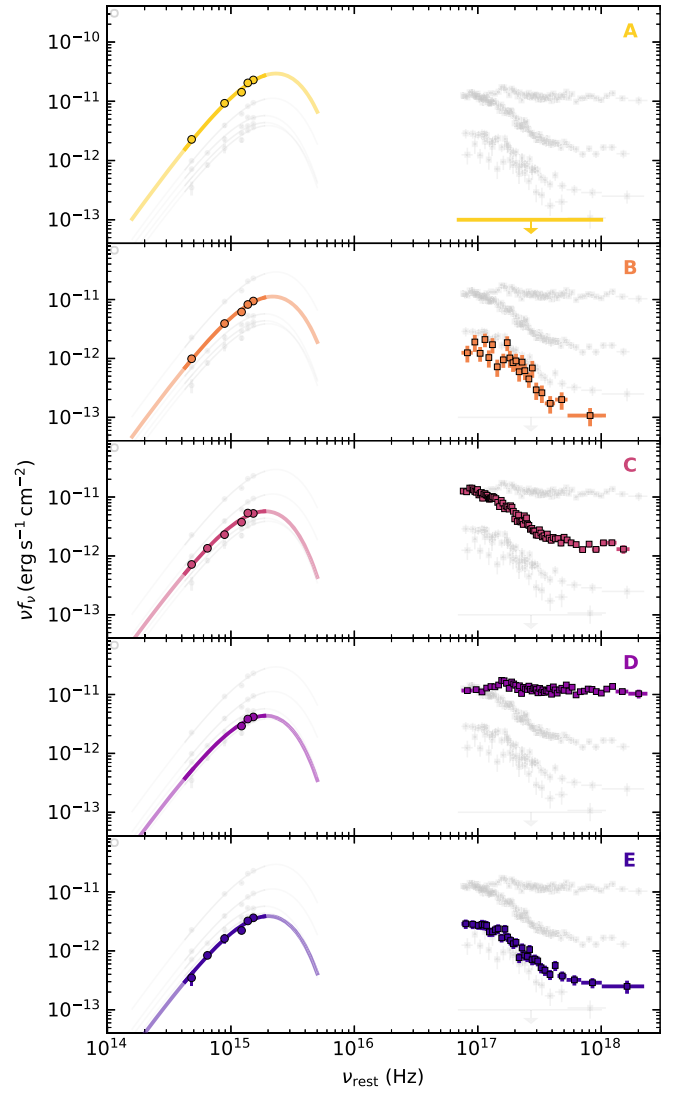


Figure 17. Typical SEDs of AT2021ehb in five phases. The data has been corrected for extinction (in UV/optical) and column density absorption (in the X-ray). The solid lines are the blackbody fits to UV/optical data.

$$= \frac{L_{\nu}(\nu_1)}{\nu_1^{\alpha_{\text{OSX}}}} \times \begin{cases} \frac{\nu_2^{\alpha_{\text{OSX}}+1} - \nu_1^{\alpha_{\text{OSX}}+1}}{\alpha_{\text{OSX}} + 1} & \text{if } \alpha_{\text{OSX}} \neq -1 \\ \ln(\nu_2/\nu_1) & \text{if } \alpha_{\text{OSX}} = -1 \end{cases} \quad (6)$$

where $\nu_1 = 10^{15.08}$ Hz, $\nu_2 = 10^{17.08}$ Hz. In this range, we assume that the uncertainty of L is $0.3L$.

From 0.5 keV to 10 keV, we calculate the luminosity by converting the 0.3–10 keV XRT net count rate to Galactic absorption corrected 0.5–10 keV luminosity using the scaling factors derived in Section 4.4.5.

Note that for the first four Swift epochs, since X-rays were not detected, we use the UV/optical blackbody luminosity L_{bb} as an approximation of L_{bol} .

The evolution of $\log L_{\text{bol}}$ as a function of α_{OX} is shown in Figure 19. The data points are color coded by their phases (from A to E; see Figure 16). The right y-axis converts L_{bol} to the Eddington ratio $\lambda_{\text{Edd}} \equiv L_{\text{bol}}/L_{\text{Edd}}$. For pure hydrogen, an M_{BH} of $10^{7.03} M_{\odot}$ (Section 3.1) implies an Eddington luminosity of $L_{\text{Edd}} \approx 10^{45.13}$ erg s $^{-1}$. We further discuss this figure in Section 5.5. The maximum luminosity was reached at

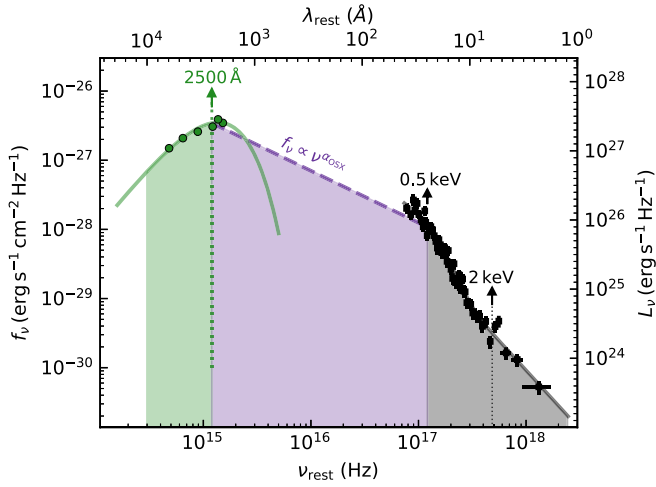


Figure 18. A snapshot SED of AT2021ehb at $\delta t \approx 147$ days. The data has been corrected for extinction (in UV/optical) and Galactic absorption (in the X-ray). The solid lines are the blackbody fits to UV/optical data (Section 4.1) and the XRT “s3” spectrum best-fit model (Section 4.4.5). The shaded region shows that the L_{bol} is calculated in three energy ranges (see the text).

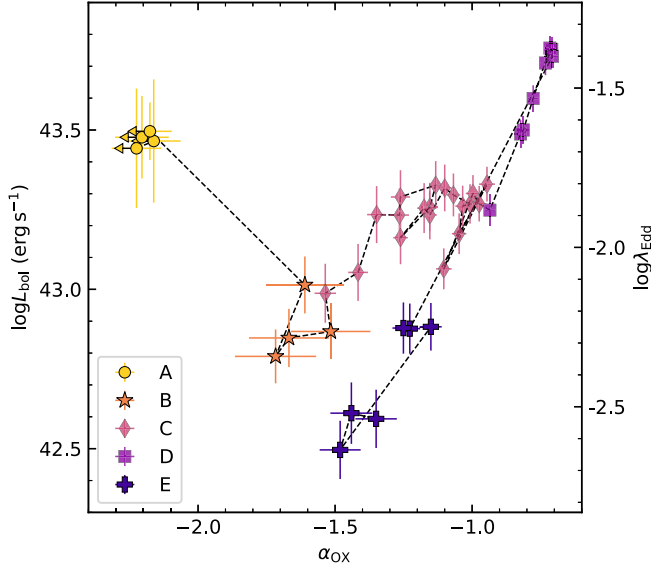


Figure 19. The bolometric luminosity L_{bol} as a function of α_{OX} . L_{bol} is converted to λ_{Edd} assuming $\log(M_{\text{BH}}/M_{\odot}) = 7.03$ (Section 3.1). Note that the uncertainty of λ_{Edd} should be greater than the uncertainty of L_{bol} by 0.44 dex (i.e., the uncertainty of M_{BH}), which is not included in the figure.

$\delta t = 253$ days, with $L_{\text{bol}} = (7.94 \pm 0.66) \times 10^{43}$ erg s $^{-1}$ and $\lambda_{\text{Edd}} = 6.0_{-3.8}^{+10.4}\%$. As a cautionary note, the relatively low value of λ_{Edd} ($< 16\%$) does not necessarily imply that the accretion is in the sub-Eddington regime, as the TDE broadband SED may peak in the extreme-UV (EUV) band (Dai et al. 2018; Mummery & Balbus 2020).

5. Discussion

Hereafter we define $M_7 \equiv M_{\text{BH}}/(10^7 M_{\odot})$, $\dot{m} \equiv \dot{M}_{\text{acc}}/\dot{M}_{\text{Edd}}$, $\dot{M}_{\text{Edd}} \equiv L_{\text{Edd}}/(\eta c^2)$, $\eta_{-1} \equiv \eta/10^{-1}$, where \dot{M}_{acc} is the mass accretion rate and η is the accretion radiative efficiency. With $M_7 \approx 1$, the gravitational radius is $R_{\text{g}} = GM_{\text{BH}}/c^2 \approx 10^{12.20}$ cm. For a solar-type star, the tidal radius is $R_{\text{T}} = 10^{13.19}$ cm $\approx 10R_{\text{g}}$, within which the tidal force exceeds the star’s self-gravity (Rees 1988).

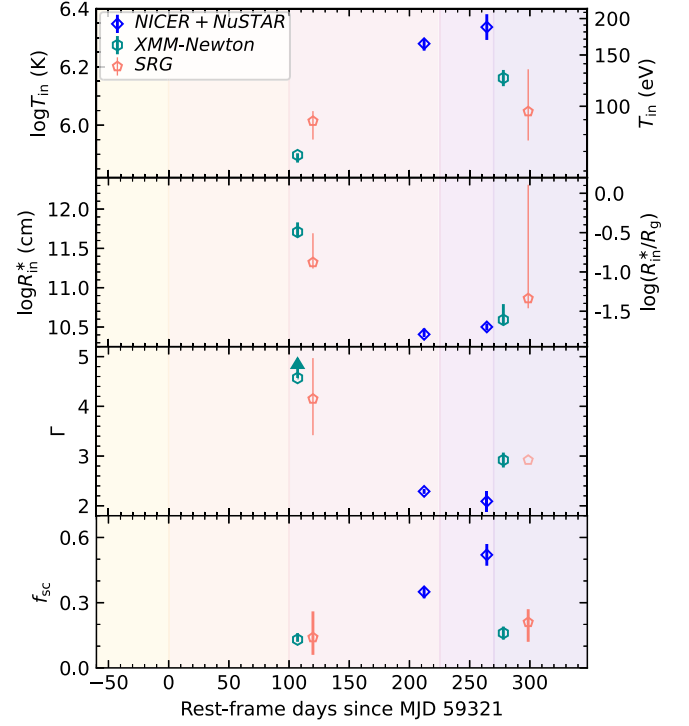


Figure 20. Evolution of best-fit X-ray spectral parameters, including $\log T_{\text{in}}$ and $\log R_{\text{in}}^*$ in the `diskbb` component (top two panels), Γ and f_{sc} in the `simpl` component (third and fourth panels). Note that the uncertainty of $\log(R_{\text{in}}^*/R_{\text{g}})$ is greater than the uncertainty of R_{in}^* by 0.44 dex (i.e., the uncertainty of M_{BH} ; Section 3.1), which is not included in the figure. Data are from model (1a) in Table 4, model (2a) in Table 5, Table 6, and Table 7. For parameters in model (2a), we assume an uncertainty of 10%. Fixed values are shown as semitransparent symbols. Background colors follow the scheme shown in Figure 16.

5.1. Origin of the Soft X-Ray Emission

The soft X-ray emission of many TDEs has been attributed to the inner regions of an accretion disk (Saxton et al. 2020). Assuming $R_{\text{in}} \approx 6R_{\text{g}} \approx 10^{13}$ cm, the maximum effective temperature of an optically thick, geometrically thin accretion disk is $T_{\text{eff}} \approx 20 \left(\frac{\dot{m}}{M_7 \eta_{-1}} \right)^{1/4}$ eV (Shakura & Sunyaev 1973). With a maximum black hole spin of $a \rightarrow 1$, $R_{\text{in}} \rightarrow R_{\text{g}}$, and $T_{\text{eff}} \approx 78 \left(\frac{\dot{m}}{M_7 \eta_{-1}} \right)^{1/4}$ eV. The top panel of Figure 20 shows that in phase D, when the X-ray spectrum is the hardest, the measured T_{in} is ~ 2.5 times greater than the maximum allowed T_{eff} . This high color temperature causes the inferred disk radius $R_{\text{d,in}} = R_{\text{in}}^*/\sqrt{\cos i}$ to be much less than R_{g} throughout the evolution. The projection factor $\sqrt{\cos i}$ should not be much less than unity, since for a nearly edge-on viewing angle, the X-rays from the inner disk will be obscured by the gas at larger radii. The relativistic disk reflection model (2c) also suggests $\sqrt{\cos i} = 0.85_{-0.07}^{+0.06}$. We note that disk radii much less than R_{g} have also been inferred in a few other X-ray bright TDEs (see, e.g., Figure 8 of Gezari 2021).

This discrepancy may be due to Compton scattering (Shimura & Takahara 1995), which makes the measured temperature greater than the effective inner disk temperature by a factor of f_{c} (Davis & El-Abd 2019), i.e., $T_{\text{in}} = f_{\text{c}} T_{\text{eff}}$. The physical reason is that, as the X-ray photons propagate in the vertical direction away from the disk mid-plane, the color temperature is determined by the thermalization depth

(corresponding to the last absorption), which could be located at a high scattering optical depth $\tau \gg 1$ —this causes T_{in} to be higher than T_{eff} by a factor of $\sim \tau^{1/4}$. As a result of ongoing fallback, the vertical structure of the TDE disk (see Bonnerot et al. 2021) is likely substantially different from the standard thin disk as studied by Davis & El-Abd (2019), who concluded $f_c \lesssim 2$, so the color correction factor may be different. More detailed radiative transport calculations in the TDE context are needed to provide a reliable f_c based on first principles.

Another possible reason for the seemingly small disk radii is that a scattering dominated, Compton-thick gas layer can suppress the X-ray flux without causing any significant change to the spectral shape. For a spatially uniform layer, the transmitted flux is exponentially suppressed for a large scattering optical depth $\gg 1$. A more likely configuration is that the layer is like an obscuring wall with small holes where a fraction of the source X-rays can get through, and the rest of the area contributes negligibly to the observed flux. In this scenario, the inferred disk radius is reduced by a factor of the square root of the transmitted over emitted fluxes.

5.2. Implications of the Hard X-Ray Emission

Hard X-rays can be generated by Compton up-scattering of soft X-rays from the accretion disk by the hot electrons in the (magnetically dominated) coronal regions above the disk, as is the case in AGNs and XRBs. The physical situation in TDEs is more complicated than in AGNs in that the hard X-rays must make their way out of the complex hydrodynamic structures. An X-ray photon undergoes $\sim \tau^2$ electron scatterings as it propagates through a gas slab of Thomson optical depth τ . In each scattering, the photon loses a fraction $E_\gamma/m_e c^2$ of its energy (where E_γ is the photon energy) as a result of Compton recoil, and hence the cumulative fractional energy loss is $\sim \tau^2 E_\gamma/m_e c^2$. This means that photons above an energy threshold of $\sim 1 \text{ keV} (\tau/20)^{-2}$ will be Compton down-scattered by the gas.

Our NuSTAR observations clearly detected hard X-ray photons up to 30 keV, which requires that the optical depth along the pathways of these photons from the inner disk ($\gtrsim R_g \sim 10^{12.2} \text{ cm}$) to the observer is less than about 4. On the other hand, the UV/optical emission indicates that the reprocessing layer is optically thick up to a radius of the order of $R_{\text{bb}} \sim 10^{14} \text{ cm}$. Therefore, our observations favor a highly nonspherical system—there are viewing angles that have very large optical depths such that most X-ray photons are absorbed (and reprocessed into the UV/optical bands), and there are other viewing angles with scattering optical depth $\tau \lesssim 4$ so that hard X-ray photons can escape.

5.3. X-Ray Spectral Evolution

5.3.1. Soft to Hard Transition: Corona Formation

The top two panels of Figure 20 show that, during the soft \rightarrow hard transition, AT2021ehb’s inferred inner disk radius “moves” inward. We find that the main cause of this behavior is that the inner disk temperature increases with time as the spectrum hardens. The gradual hardening is consistent with a picture where it takes $\sim 10^2$ days to build up the magnetically dominated hot corona region. It is possible that the initially weak magnetic fields in the bound debris are amplified by differential rotation of the disk and the magnetorotational instability (Balbus & Hawley 1991; Miller & Stone 2000).

5.3.2. Hard to Soft Transition: Thermal–Viscous Instability?

The rapid X-ray flux drop (D \rightarrow E) is likely due to a state transition in the innermost regions of the accretion disk. Under the standard α -viscosity prescription where the viscous stress is proportional to the total (radiation + gas) pressure (Shakura & Sunyaev 1973), the disk undergoes a thermal–viscous instability as the accretion rate drops from super- to sub-Eddington regimes (Lightman & Eardley 1974; Shakura & Sunyaev 1976). This instability causes the disk material to suddenly transition from a radiation pressure-dominated to gas pressure-dominated state on a sound-crossing timescale, and the consequence is that the disk becomes much thinner and hence the accretion rate drops. Shen & Matzner (2014) considered the thermal–viscous instability in the TDE context but concluded that the instability should occur within a few months since the disruption and the accretion rate drops by several orders of magnitude—these, taken at face value, are inconsistent with our observations. More detailed work on the disk evolution is needed to draw a firm conclusion. Here, we provide two arguments for the disk state transition explanation.

First, TDEs with relativistic jets (e.g., Bloom et al. 2011; Burrows et al. 2011; Cenko et al. 2012; Pasham et al. 2015) also show a sharp drop in X-ray luminosity 200 to 300 days (in the rest frame) after the discovery and that has been interpreted as the thick-to-thin transition of the inner disk (Tchekhovskoy et al. 2014). Second, from the mass fallback rate $\dot{M}_{\text{fb}} \simeq M_*/3P_{\text{min}}(t/P_{\text{min}})^{-5/3}$ (M_* being the stellar mass and P_{min} being the minimum period of the fallback material), one can estimate the time t_{Edd} at which the fallback rate drops below the Eddington accretion rate of $\sim 10L_{\text{Edd}}/c^2$, and the result is (Lu & Kumar 2018)

$$t_{\text{Edd}} \simeq 309 \text{ d } M_{\text{h},7}^{-2/5} \left(\frac{M_*}{M_\odot} \right)^{(1+3q)/5}, \quad (7)$$

where we have taken the normal mass–radius relation of main-sequence stars $R_* \simeq R_\odot (M_*/M_\odot)^q$ ($q = 0.8$ below one solar mass stars and $q = 0.57$ above one solar mass stars). We expect the inner disk to collapse into a thin state on the timescale t_{Edd} , under the condition that an order-unity fraction of the fallback rate directly reaches near the innermost regions of the disk. We note that the condition is satisfied for $a \approx 10^7 M_\odot$ MBH since the tidal radius is only $\approx 10R_g$ for a solar-type star.

If the rapid X-ray flux drop (D \rightarrow E) is indeed caused by a disk state transition, then after the transition, the disk mass will accumulate over time due to ongoing fallback. This causes the accretion rate to increase, and eventually the disk briefly goes back to a thick state (with a very short viscous time) followed by another transition to the thin state. This is qualitatively consistent with the second rapid X-ray flux decline at $\delta t \approx 325$ days (E1 \rightarrow E2 in Figure 16).

5.4. Unusual UV/optical Behavior

5.4.1. Featureless Optical Spectrum

As shown in Section 4.2, AT2021ehb’s optical spectroscopic properties are dissimilar to the majority of previously known TDEs (i.e., H-rich, He-rich, N-rich, Fe-rich; Leloudas et al. 2019; van Velzen et al. 2021; Wevers et al. 2019a). It is most similar to a few recently reported TDEs with blue and featureless spectra (Brightman et al. 2021; Hammerstein et al. 2022). Hammerstein et al. (2022) found that compared with

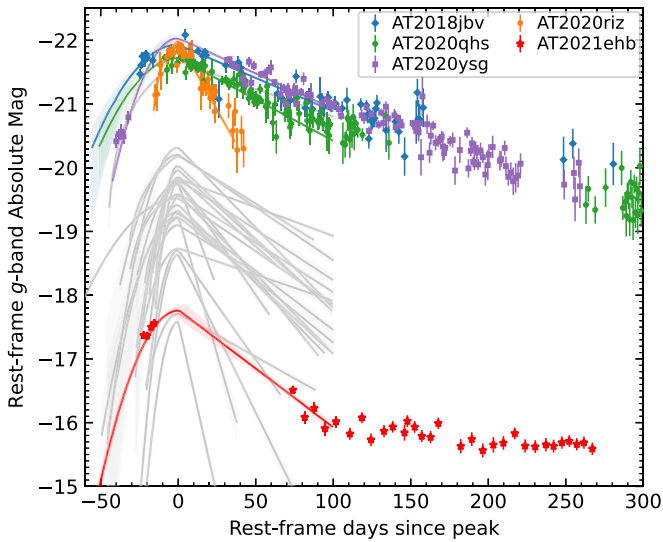


Figure 21. Rest-frame g -band light curve of AT2021ehb compared with that of the 30 TDEs presented by Hammerstein et al. (2022). The solid lines show the best-fit models (see the text for details). Data points and labeled names are only shown for TDEs with no discernible optical broad lines.

TDEs that develop broad emission lines, the UV/optical emission of four featureless events have larger peak L_{bb} , peak T_{bb} , and peak R_{bb} .

Figure 21 compares the rest-frame g -band light curve of AT2021ehb with 30 TDEs from phase I of ZTF (Hammerstein et al. 2022). Solid lines are the results of fitting the multiband light curves ($\delta t < 100$ days) with a Gaussian rise + exponential decay model (see Section 5.1 of van Velzen et al. 2021). We highlight the TDEs lacking line features by plotting the data as colored symbols. Here we have chosen an observing band with good temporal sampling, and converted the observations in this band into $\nu_0 = 6.3 \times 10^{14}$ Hz by performing a color correction.

Our study suggests that not all featureless TDEs are overluminous. In fact, the peak g -band magnitude ($M_{g,\text{peak}}$) and peak L_{bb} of AT2021ehb are faint compared with other optically selected TDEs (Figure 6, Figure 21). It is unclear whether $M_{g,\text{peak}}$ of the TDE-featureless class forms a continuous or bimodal distribution between -17 and -22 . This question will be addressed in a forthcoming publication (Y. Yao et al. 2022, in preparation). A detailed analysis of Hubble Space Telescope UV spectroscopy (E. Hammerstein et al. 2022, in preparation) will be essential to reveal if AT2021ehb exhibits any spectral lines in the UV.

5.4.2. Origin of the NUV/optical Emission

Here we discuss possible origins of AT2021ehb's NUV/optical emission: stream self-crossing shock, reprocessing, and thermal emission from disk accretion.

In the self-crossing shock model, since the radius of the self-crossing shock is determined by the amount of general relativistic apsidal precession as given by the pericenter of the initial stellar orbit (Dai et al. 2015), we expect the power of the self-crossing shock to track the fallback rate and decay with time as $\sim t^{-5/3}$. This is inconsistent with the flat light curve observed in AT2021ehb in the UV/optical bands (phase C–E), unless there is an additional mechanism that modulates the radiative efficiency of the self-crossing shock such that it roughly cancels the effects of the dropping shock dissipation power. Therefore, the energy dissipated by the stream–stream

collision cannot be the primary source of emission during the plateau phase, although it may contribute to the early-time UV/optical emission.

In the reprocessing model, the nature of the reprocessing layer could originate from either a disk wind (Strubbe & Quataert 2009; Miller 2015; Dai et al. 2018; Parkinson et al. 2022; Thomsen et al. 2022) or an outflow from the self-crossing shock (Jiang et al. 2016; Lu & Bonnerot 2020). The outflow scenario is favored for two reasons. First, a radiation pressure-driven disk wind originates from the innermost regions of the disk and the wind density is geometrically diluted as it propagates to a distance of the order of $R_{\text{bb}} \sim 10^{14}$ cm, whereas the outflow from the self-crossing shock is expected to be much denser near the self-crossing point and is hence more capable of reprocessing the hard emission from the disk (Bonnerot et al. 2021). Second, as the accretion flow goes from super-Eddington to sub-Eddington (Section 5.3.2), one may expect the reduction in radiation pressure to reduce the strength of the wind outflows. The fact that the UV/optical luminosity only slightly decreases from phase D to phase E suggests that the reprocessing layer is not sensitive to the innermost accretion flow.

Finally, if the UV/optical emission is powered by disk accretion, then the outer disk radius must be located at $\gtrsim 10R_{\text{T}} \approx 100R_{\text{g}}$. Recent simulations show that it is possible that a small fraction of the bound debris circularizes at $\sim 10R_{\text{T}}$ (Bonnerot et al. 2021), but the accretion power at such large radii may be too low to produce the observed UV/optical emission, since the outermost regions of the disk are expected to be geometrically thin (due to efficient radiative cooling) with a very long viscous time. More detailed disk evolution modeling is needed to evaluate this possibility.

To summarize, we infer that the early-time UV/optical light may be thermal radiation emitted at the photosphere of a stream–stream collision shock. The late-time UV/optical emission likely comes from reprocessing by the outflow launched from the self-crossing shock, although thermal emission from the outer regions of an accretion flow is not ruled out.

5.5. Comparison to Other Accreting Black Holes

In stellar-mass black hole XRB outbursts, some objects are observed to transition between a soft disk-dominated state (SDS) and a hard Comptonized state (HCS). In the SDS of XRBs, the inner radius ($R_{\text{in,d}}$) of an optically thick, geometrically thin disk stays around the ISCO of $R_{\text{ISCO}} \sim \text{a few} \times R_{\text{g}}$. When the outbursts transition to the HCS, \dot{M}_{acc} decreases, and $R_{\text{in,d}}$ progressively moves outwards to $\sim \text{few} \times 100R_{\text{g}}$, leaving a radiatively inefficient, advection-dominated accretion flow (Yuan et al. 2005; Yuan & Narayan 2014). At the same time, a region of hot corona is formed close to the BH (Done et al. 2007). For MBH accretors, Seyferts have been proposed as the high- M_{BH} analogs of XRBs in the SDS, whereas low-luminosity AGNs and low-ionization nuclear emission-line regions are considered similar to XRBs in the HCS (Falcke et al. 2004).

In Section 5.3.2, we propose that in phases B–D, the accretion flow of AT2021ehb is in a radiation-trapped, super-Eddington regime (see, e.g., Figure 2 of Narayan & Quataert 2005), which is different from the typical sub-Eddington X-ray states observed in AGNs and XRBs. Such a difference is further corroborated by two properties. First, on

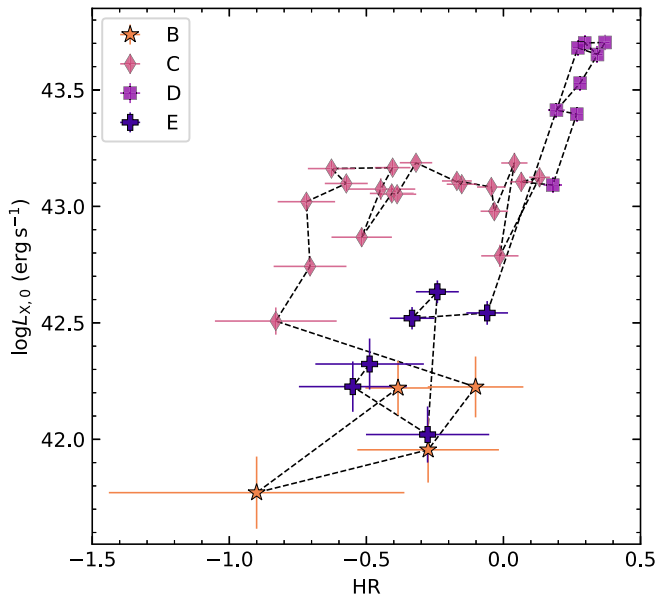


Figure 22. Galactic extinction-corrected 0.3–10 keV X-ray luminosity ($L_{X,0}$) as a function of hardness ratio for Swift/XRT detections only.

the hardness–intensity diagram (HID; see Figure 22), the evolution of AT2021ehb is neither similar to the “turtlehead” pattern observed in XRBs (Fender et al. 2004; Munoz-Darias et al. 2013; Tetarenko et al. 2016), nor similar to the “brighter when softer” trend observed in X-ray bright AGNs (Auchettl et al. 2018). On the $L_{\text{bol}}-\alpha_{\text{OX}}$ diagram (Figure 19), its evolution is also different from that observed in CLAGNs (Ruan et al. 2019). Second, in the canonical hard state (i.e., sub-Eddington accretion rates), there is a correlation among radio luminosity, X-ray luminosity, and M_{BH} , which applies to both XRBs and hard-state AGNs (Merloni et al. 2003; Falcke et al. 2004). A recent fit to this “fundamental plane of black hole activity” was provided by Gültekin et al. (2019):

$$(1.09 \pm 0.10)R = (\log M_7 - 1) - (0.55 \pm 0.22) - (-0.59_{-0.15}^{+0.16})X, \quad (8)$$

where $R \equiv \log[L_{5 \text{ GHz}}/(10^{38} \text{ erg s}^{-1})]$ and $X \equiv \log[L_{2-10 \text{ keV}}/(10^{40} \text{ erg s}^{-1})]$. In the hard state of AT2021ehb, the 2–10 keV luminosity in the Swift/XRT “s6” spectrum gives $X = 2.96 \pm 0.02$. Using Equation (8), the expected 5 GHz radio luminosity on the fundamental plane is $\log[L_{5 \text{ GHz}}/(\text{erg s}^{-1})] = R + 38 = 38.21 \pm 0.59$. The uncertainty of R is calculated from the distribution of 10^5 MC trials. Using our radio limit at $\delta t = 228$ days (Table 2) and assuming a flat radio spectrum of $f_\nu \propto \nu^0$, we find a 5 GHz equivalent radio upper limit of $\log[L_{5 \text{ GHz}}/(\text{erg s}^{-1})] < 35.76$. According to Gültekin et al. (2019), the scatter on the fundamental plane correlation is a factor of ~ 7.6 in the $L_{5 \text{ GHz}}$ direction (or ~ 10 in the M_{BH} direction), which is not enough to solve the discrepancy. This again argues that AT2021ehb is not in a canonical hard state where we would expect a radio jet to be launched.

The radio behavior of BH binaries at the Eddington accretion rates might be more relevant to AT2021ehb (at least in phases B–D). A few XRBs get above the Eddington limit for brief periods, when they are seen to undergo a sequence of bright radio flares for a short period of time. Examples include the 2015 outburst of V404 Cygni (Tetarenko et al. 2017, 2019) and

the ultraluminous X-ray source in M31 (Middleton et al. 2013). In AT2021ehb, the slow cadence of our radio follow-up observations does not allow us to rule out the existence of such radio flares, which last for hours to weeks, not months.

Finally, we note that the evolution of the X-ray properties of AT2021ehb are different from a few other TDEs. For example, Wevers et al. (2021) constructed the $\log \lambda_{\text{Edd}}-\alpha_{\text{OX}}$ diagram for AT2018fyk, finding that the 2 keV (corona) emission is stronger when λ_{Edd} is lower. Figure 19 shows that this is clearly not the case for AT2021ehb. Separately, Hinkle et al. (2021) studied the evolution of AT2019azh on the canonical HID, showing that when the X-ray luminosity is higher, the X-ray spectrum is softer. Figure 22 shows that AT2021ehb does not follow this trend either. It remains to be seen whether AT2021ehb is peculiar among the sample of optically selected TDEs with significant X-ray spectral evolution. To this end, constructing a systematically selected sample and analyzing the multiwavelength data in a homogeneous fashion is the key.

6. Conclusion

We have presented an extensive multiwavelength study of the TDE AT2021ehb. Its peak 0.3–10 keV flux of ~ 1 mCrab is brighter than any other non-jetted TDE in the literature, allowing us to obtain a series of high-quality X-ray spectra, including the first hard X-ray spectrum of a non-jetted TDE up to 30 keV. The detection of hard X-ray photons favors a highly aspherical geometry (Section 5.2), and detailed modeling of the NICER +NuSTAR spectrum shows evidence of relativistic disk reflection (Section 4.4.2).

The emission from the self-crossing shock itself might contribute to the early-time UV/optical emission, while the post-peak (phase C–E) emission is either dominated by reprocessing of X-ray photons by the outflow launched from the shock, or by thermal emission in the outer regions of an accretion flow (Section 5.4.2). More detailed hydrodynamic and radiative transfer calculations (e.g., Roth et al. 2016) are needed to test if such scenarios can reproduce the observed UV/optical plateau and the featureless optical spectra.

We observed a soft \rightarrow hard \rightarrow soft spectral transition in the X-ray. The initial soft-to-hard transition happened gradually over ~ 170 days. A possible explanation is that magnetic fields grow with time due to differential rotation, resulting in the formation of a magnetically dominated hot corona (Section 5.3.1). The bolometric luminosity of AT2021ehb is the highest when the X-ray spectrum is the hardest—a property that is different from XRBs, X-ray bright AGNs, and many other TDEs (Section 5.5). The latter hard-to-soft transition happened drastically within 3 days at $\delta t \approx 272$ days, and might be due to thermal–viscous instability in the inner disk (Section 5.3.2). Such an instability typically occurs when $L_{\text{bol}} \sim 0.3L_{\text{Edd}}$ (Tchekhovskoy et al. 2014). This requires that most of the luminosity of AT2021ehb is emitted in the EUV band that is not observed.

Systems similar to AT2021ehb are excellent targets for X-ray telescopes to study the real-time formation of the accretion disk and corona around MBHs. The detection of relativistic disk reflection features demonstrates the possibility of constraining the spin of normally quiescent MBHs via reflection spectroscopy—an opportunity enabled by combining modern time-domain surveys with systematic multiwavelength follow-up observations.

We are grateful to the NuSTAR, NICER, Swift, XMM-Newton, and VLA teams for making this observing campaign possible. We thank the anonymous referee for constructive comments and suggestions. We thank Julian Krolik for providing comments on an early version of this manuscript. We thank Erin Kara, Renee Ludlam, Guglielmo (Gullo) Mastroserio, and Riley Connors for helpful discussions on the NuSTAR and NICER spectral fitting. We thank Murray Brightman and Hannah Earnshaw for discussions on disk reflection and super-Eddington accretion.

Y.Y. acknowledges support from NASA under award No. 80NSSC22K0574. W.L. is supported by the Lyman Spitzer, Jr. Fellowship at Princeton University. This work was supported by the Australian government through the Australian Research Council’s Discovery Projects funding scheme (DP200102471). M.N. is supported by the European Research Council (ERC) under the European Unions Horizon 2020 research and innovation program (grant agreement No. 948381) and by a Fellowship from the Alan Turing Institute. E.C.K. acknowledges support from the G.R.E.A.T. research environment funded by *Vetenskapsrådet*, the Swedish Research Council, under project No. 2016-06012, and support from The Wenner-Gren Foundations.

This work has made use of data from the NuSTAR mission, a project led by Caltech, managed by NASA/JPL, and funded by NASA. This research has made use of the NuSTAR Data Analysis Software (NuSTARDAS), jointly developed by the ASI Science Data Center (ASDC, Italy) and Caltech (USA).

This work is based on observations obtained with the Samuel Oschin Telescope 48 inch and the 60 inch Telescope at the Palomar Observatory as part of the Zwicky Transient Facility (ZTF) project. ZTF is supported by the National Science Foundation under grant No. AST-2034437 and a collaboration including Caltech, IPAC, the Weizmann Institute of Science, the Oskar Klein Center at Stockholm University, the University of Maryland, Deutsches Elektronen-Synchrotron and Humboldt University, the TANGO Consortium of Taiwan, the University of Wisconsin at Milwaukee, Trinity College Dublin, Lawrence Livermore National Laboratories, IN2P3, University of Warwick, Ruhr University Bochum, and Northwestern University. Operations are conducted by COO, IPAC, and UW. The ZTF forced-photometry service was funded under the Heising-Simons Foundation grant No. 12540303 (PI: Graham).

SED Machine is based upon work supported by the National Science Foundation under grant No. 1106171. This work used observations with the eROSITA telescope on board the SRG observatory. The SRG observatory was built by Roskosmos with the participation of the Deutsches Zentrum für Luft- und

Raumfahrt (DLR). The SRG/eROSITA X-ray telescope was built by a consortium of German Institutes led by MPE, and supported by DLR. The SRG spacecraft was designed, built, launched, and is operated by the Lavochkin Association and its subcontractors. The eROSITA data used in this work were processed using the eSASS software system developed by the German eROSITA consortium and proprietary data reduction and analysis software developed by the Russian eROSITA Consortium.

This work made use of data supplied by the UK Swift Science Data Centre at the University of Leicester.

The National Radio Astronomy Observatory is a facility of the National Science Foundation operated under cooperative agreement by Associated Universities, Inc.

Software: `astropy` (Astropy Collaboration et al. 2013), `CASA` (McMullin et al. 2007), `emcee` (Foreman-Mackey et al. 2013), `heasoft` (Heasarc 2014), `LPipe` (Perley 2019), `matplotlib` (Hunter 2007), `Prospector` (Johnson et al. 2021), `pwkit` (Williams et al. 2017), `python-fsps` (Foreman-Mackey et al. 2014), `relxill` (García et al. 2014; Dauser et al. 2014), `scipy` (Virtanen et al. 2020), `xspec` (Arnaud 1996).

Facilities: XMM, NuSTAR, Swift, NICER, SRG, PO:1.2 m, PO:1.5 m, Hale, Keck:I (LRIS), Keck: II (ESI), LDT, VLA.

Appendix A Supplementary Tables

A.1. Photometry and Observing Logs

UV and optical photometry are presented in Table 8. Swift/XRT observations are summarized in Table 9.

Table 8
UV and Optical Photometry of AT2021ehb

MJD	Instrument	Filter	f_ν (μJy)	σ_{f_ν} (μJy)
59250.1643	ZTF	<i>r</i>	−3.31	12.48
59250.2031	ZTF	<i>g</i>	2.07	10.91
59299.0783	UVOT	<i>uvw1</i>	567.68	27.76
59299.0798	UVOT	<i>U</i>	551.85	41.60
59299.0808	UVOT	<i>B</i>	487.52	76.95
59299.0831	UVOT	<i>uvw2</i>	587.34	22.36
59299.0855	UVOT	<i>V</i>	260.66	146.91
59299.0875	UVOT	<i>uvm2</i>	528.68	19.49

Note. f_ν is observed flux density before extinction correction.

(This table is available in its entirety in machine-readable form.)

Table 9
Log of Swift/XRT Observations of AT2021ehb

obsID	Start Date	δt (days)	Exp. (s)	Net Count Rate (count s ⁻¹)	f_X (10 ⁻¹³ erg s ⁻¹ cm ⁻²)	$f_{X,0}$ (10 ⁻¹³ erg s ⁻¹ cm ⁻²)
14217001	2021-03-26.0	-21.6	2669	<0.0019	<0.66	<1.25
14217003	2021-03-28.2	-19.4	1475	<0.0027	<0.96	<1.82
14217004	2021-03-31.0	-16.7	1683	<0.0024	<0.84	<1.59
14217005	2021-04-02.0	-14.7	1336	<0.0030	<1.06	<2.01
14217006	2021-07-01.2	+73.9	4078	0.0339 ± 0.0029	12.01 ± 3.21	22.73 ± 6.08
14217007	2021-07-09.8	+82.3	1366	0.0120 ± 0.0030	4.27 ± 1.52	8.08 ± 2.88
14217008	2021-07-16.1	+88.5	1348	0.0184 ± 0.0037	6.52 ± 2.11	12.34 ± 4.00
14217009	2021-07-23.1	+95.4	1141	0.0343 ± 0.0056	12.13 ± 3.65	22.96 ± 6.90
14217010	2021-07-30.1	+102.3	1366	0.0502 ± 0.0061	16.57 ± 2.23	44.04 ± 5.92
14217011	2021-08-08.1	+111.1	1925	0.0863 ± 0.0067	28.44 ± 2.76	75.62 ± 7.34
14217012	2021-08-15.9	+118.8	1653	0.1635 ± 0.0100	53.90 ± 4.54	143.32 ± 12.08
14217013	2021-08-22.1	+124.8	2065	0.1958 ± 0.0098	64.56 ± 4.94	171.64 ± 13.13
14217014	2021-08-30.9	+133.5	1583	0.2268 ± 0.0120	74.78 ± 5.87	198.82 ± 15.61
14217015	2021-09-05.5	+139.0	1830	0.2548 ± 0.0119	94.07 ± 7.27	200.69 ± 15.51
14217016	2021-09-12.8	+146.2	641	0.2061 ± 0.0180	76.09 ± 8.13	162.34 ± 17.35
14217017	2021-09-15.0	+148.4	1503	0.1281 ± 0.0093	47.29 ± 4.51	100.90 ± 9.63
14217018	2021-09-19.7	+153.0	1580	0.1974 ± 0.0112	72.90 ± 6.12	155.52 ± 13.05
14217019	2021-09-24.2	+157.4	2045	0.1959 ± 0.0098	72.33 ± 5.76	154.31 ± 12.28
14217020	2021-09-30.4	+163.5	1867	0.2675 ± 0.0120	98.74 ± 7.54	210.67 ± 16.09
14217021	2021-10-05.5	+168.5	1595	0.2775 ± 0.0132	104.81 ± 9.01	170.40 ± 14.65
14217022	2021-10-20.2	+182.9	1618	0.2865 ± 0.0134	108.22 ± 9.24	175.94 ± 15.02
14217023	2021-10-27.4	+190.0	1480	0.2698 ± 0.0136	101.93 ± 8.91	165.71 ± 14.48
14217024	2021-11-03.5	+197.0	2010	0.2124 ± 0.0103	80.23 ± 6.94	130.44 ± 11.29
14217025	2021-11-10.7	+204.0	1286	0.3132 ± 0.0157	149.64 ± 15.02	210.15 ± 21.10
14217026	2021-11-17.2	+210.4	1813	0.1251 ± 0.0084	59.75 ± 6.57	83.92 ± 9.23
14217027	2021-11-24.7	+217.7	1957	0.2718 ± 0.0119	129.86 ± 12.64	182.38 ± 17.75
14217028	2021-12-01.5	+224.4	1967	0.2600 ± 0.0116	124.20 ± 12.14	174.42 ± 17.05
14217029	2021-12-08.1	+230.9	2317	0.2596 ± 0.0107	126.84 ± 9.59	168.93 ± 12.77
14217030	2021-12-15.2	+237.9	2010	0.5234 ± 0.0162	255.79 ± 18.06	340.66 ± 24.05
14217031	2021-12-20.3	+242.9	1293	0.5445 ± 0.0206	266.11 ± 19.65	354.40 ± 26.17
14217032	2021-12-25.6	+248.2	1395	0.7108 ± 0.0227	347.35 ± 24.66	462.59 ± 32.84
14217033	2021-12-30.5	+253.0	1371	0.9721 ± 0.0268	551.93 ± 41.79	691.67 ± 52.37
14217034	2022-01-04.5	+257.8	1410	0.9675 ± 0.0263	549.33 ± 41.53	688.41 ± 52.05
14217035	2022-01-09.2	+262.4	1361	0.8629 ± 0.0253	489.92 ± 37.43	613.96 ± 46.91
14217036	2022-01-14.7	+267.9	1423	0.9218 ± 0.0256	523.38 ± 39.68	655.88 ± 49.72
14217041	2022-02-23.1	+306.6	2594	0.0745 ± 0.0054	26.05 ± 3.06	47.73 ± 5.60
14217042	2022-03-02.2	+313.5	3888	0.0706 ± 0.0043	24.72 ± 2.73	45.29 ± 5.01
14217043	2022-03-09.7	+320.9	2766	0.0918 ± 0.0058	32.11 ± 3.59	58.83 ± 6.58
14217044	2022-03-16.1	+327.2	2956	0.0122 ± 0.0022	5.03 ± 1.40	14.35 ± 3.98
14217045	2022-03-23.0	+334.0	3263	0.0197 ± 0.0025	8.08 ± 2.01	23.04 ± 5.73
14217046	2022-03-30.5	+341.3	2354	0.0246 ± 0.0033	10.11 ± 2.55	28.81 ± 7.26

Note. All measurements are given in 0.3–10 keV. f_X and $f_{X,0}$ are converted using the scaling factors derived in Table 11.

A.2. Model Fits

Table 10 presents the photospheric parameters derived from fitting a blackbody function to the UV/optical data. Note that the uncertainty of T_{bb} is only computed for “good” epochs (see details in Section 4.1).

The XRT spectral parameters are presented in Table 11.

Table 10
UV/optical Blackbody Parameters

δt (days)	L_{bb} (10^{43} erg s $^{-1}$)	R_{bb} (10^{14} cm)	T_{bb} (10^3 K)
−50.0	0.39 ± 0.15	0.91 ± 0.03	2.85
−45.0	0.67 ± 0.25	1.19 ± 0.01	2.85
−40.0	1.01 ± 0.38	1.46 ± 0.05	2.85
−30.0	2.10 ± 0.78	2.11 ± 0.04	2.85
−25.0	2.62 ± 0.96	2.36 ± 0.03	2.85
−21.5	2.77 ± 1.19	2.42 ± 0.27	2.85 ± 0.26
−19.2	2.92 ± 1.30	2.51 ± 0.29	2.84 ± 0.27
−16.7	3.00 ± 0.89	2.70 ± 0.20	2.75 ± 0.18
−14.7	3.13 ± 0.65	2.80 ± 0.14	2.73 ± 0.13
−10.0	3.31 ± 0.62	2.89 ± 0.02	2.73
70.0	1.33 ± 0.29	1.91 ± 0.02	2.67
74.7	1.12 ± 0.29	1.75 ± 0.12	2.67 ± 0.15
82.4	1.06 ± 0.86	1.45 ± 0.31	2.90 ± 0.50
88.6	1.27 ± 1.46	1.18 ± 0.34	3.36 ± 0.84
95.4	0.79 ± 0.67	1.42 ± 0.33	2.72 ± 0.48
102.3	0.55 ± 0.18	1.79 ± 0.17	2.22 ± 0.15
111.5	0.52 ± 0.12	1.70 ± 0.10	2.24 ± 0.11
119.3	0.60 ± 0.10	1.56 ± 0.07	2.43 ± 0.09
125.1	0.54 ± 0.20	1.67 ± 0.18	2.28 ± 0.18
133.6	0.50 ± 0.18	1.82 ± 0.19	2.14 ± 0.16
139.2	0.52 ± 0.13	1.80 ± 0.12	2.18 ± 0.11
147.0	0.57 ± 0.15	1.65 ± 0.11	2.32 ± 0.13
153.3	0.60 ± 0.25	1.51 ± 0.18	2.47 ± 0.22
157.9	0.57 ± 0.30	1.47 ± 0.21	2.47 ± 0.27
163.6	0.54 ± 0.19	1.50 ± 0.15	2.41 ± 0.18
168.6	0.63 ± 0.25	1.31 ± 0.14	2.68 ± 0.23
178.0	0.42 ± 0.18	1.65 ± 0.18	2.16 ± 0.20
183.1	0.44 ± 0.25	1.51 ± 0.25	2.28 ± 0.26
190.2	0.43 ± 0.22	1.55 ± 0.23	2.24 ± 0.23
197.3	0.37 ± 0.13	1.76 ± 0.17	2.02 ± 0.14
204.1	0.43 ± 0.19	1.53 ± 0.18	2.25 ± 0.20
210.5	0.44 ± 0.25	1.59 ± 0.26	2.22 ± 0.26
217.8	0.44 ± 0.20	1.56 ± 0.05	2.24
224.5	0.42 ± 0.18	1.51 ± 0.07	2.26
231.0	0.40 ± 0.17	1.44 ± 0.05	2.27
238.0	0.42 ± 0.17	1.47 ± 0.04	2.29
242.9	0.42 ± 0.16	1.45 ± 0.05	2.30
248.2	0.42 ± 0.16	1.43 ± 0.05	2.32
253.0	0.43 ± 0.16	1.43 ± 0.04	2.33
257.8	0.43 ± 0.15	1.42 ± 0.03	2.34
262.4	0.42 ± 0.14	1.39 ± 0.03	2.35
267.9	0.41 ± 0.13	1.35 ± 0.03	2.37
276.0	0.39 ± 0.12	1.29 ± 0.04	2.39
296.0	0.42 ± 0.11	1.29 ± 0.03	2.44
302.0	0.38 ± 0.11	1.22 ± 0.08	2.45 ± 0.15
306.7	0.39 ± 0.10	1.22 ± 0.02	2.45
313.7	0.39 ± 0.10	1.23 ± 0.04	2.45
320.9	0.32 ± 0.08	1.11 ± 0.04	2.45
327.5	0.26 ± 0.07	1.01 ± 0.03	2.45
334.3	0.24 ± 0.06	0.97 ± 0.03	2.45
341.4	0.25 ± 0.06	0.98 ± 0.03	2.45

Table 11
X-Ray Fluxes from Modeling of XRT Spectra

Observation	Net 0.3–10 keV Rate (count s ⁻¹)	$f_i(0.5 \text{ keV})$ (μJy)	$f_i(2 \text{ keV})$ (μJy)	$f_x(0.3\text{--}10 \text{ keV})$ ($10^{-13} \text{ erg s}^{-1} \text{ cm}^{-2}$)	$f_{x,0}(0.3\text{--}10 \text{ keV})$ ($10^{-13} \text{ erg s}^{-1} \text{ cm}^{-2}$)	$f_{x,0}(0.5\text{--}10 \text{ keV})$ ($10^{-13} \text{ erg s}^{-1} \text{ cm}^{-2}$)
s1	0.0276 ± 0.0019	1.133 ^{+0.103} _{-0.185}	0.030 ^{+0.002} _{-0.023}	9.76 ^{+1.39} _{-1.08}	18.47 ^{+2.63} _{-2.05}	11.34 ^{+0.37} _{-2.72}
s2	0.1476 ± 0.0041	9.639 ^{+0.178} _{-0.595}	0.106 ^{+0.008} _{-0.012}	48.67 ^{+1.79} _{-1.03}	129.40 ^{+4.76} _{-2.74}	48.96 ^{+1.34} _{-2.53}
s3	0.2116 ± 0.0047	10.930 ^{+0.287} _{-0.694}	0.312 ^{+0.017} _{-0.018}	78.12 ^{+2.87} _{-1.95}	166.66 ^{+6.13} _{-4.15}	86.04 ^{+1.75} _{-3.95}
s4	0.2584 ± 0.0062	7.565 ^{+0.224} _{-0.683}	0.544 ^{+0.026} _{-0.035}	97.63 ^{+3.67} _{-3.31}	158.72 ^{+5.97} _{-5.37}	109.87 ^{+2.56} _{-5.73}
s5	0.2382 ± 0.0058	5.485 ^{+0.211} _{-0.583}	0.678 ^{+0.029} _{-0.054}	113.80 ^{+5.90} _{-4.00}	159.82 ^{+8.29} _{-5.62}	127.47 ^{+3.50} _{-7.81}
s6	0.4776 ± 0.0083	8.675 ^{+0.247} _{-1.257}	1.702 ^{+0.057} _{-0.063}	233.38 ^{+8.72} _{-4.48}	310.81 ^{+11.61} _{-5.97}	256.24 ^{+7.73} _{-11.39}
s7	0.9314 ± 0.0129	14.647 ^{+0.724} _{-1.061}	3.575 ^{+0.082} _{-0.164}	528.81 ^{+20.29} _{-13.21}	662.69 ^{+25.43} _{-16.55}	579.24 ^{+11.66} _{-27.10}
s8	0.0780 ± 0.0029	2.843 ^{+0.121} _{-0.351}	0.132 ^{+0.010} _{-0.014}	27.30 ^{+1.56} _{-0.96}	50.03 ^{+2.85} _{-1.77}	30.99 ^{+1.06} _{-2.74}
s9	0.0185 ± 0.0015	1.218 ^{+0.006} _{-0.741}	0.027 ^{+0.006} _{-0.005}	7.59 ^{+1.11} _{-0.52}	21.62 ^{+3.15} _{-1.48}	6.78 ^{+0.48} _{-1.38}

Appendix B Optical Spectroscopy Instrumental/Observational Information

A log of optical spectroscopic observation is given in Table 12.

For LRIS observations, we used the 560 dichroic, the 400/3400 grism on the blue side, the 400/8500 grating on the red side, and the 1'' slit width, which gives $\sigma_{\text{inst}} \approx 173 \text{ km s}^{-1}$ on the blue side and $\sigma_{\text{inst}} \approx 126 \text{ km s}^{-1}$ on the red side. The LRIS spectra were reduced and extracted using `Lpipe` (Perley 2019).

For DBSP observations, we used the D-55 dichroic filter, the 600/4000 grating on the blue side, and the 316/7500 grating on the red side. With a slit width of 1''.5 (2''0), this gives $\sigma_{\text{inst}} \approx 106 \text{ km s}^{-1}$ ($\sigma_{\text{inst}} \approx 141 \text{ km s}^{-1}$) on the blue side and $\sigma_{\text{inst}} \approx 143 \text{ km s}^{-1}$ ($\sigma_{\text{inst}} \approx 190 \text{ km s}^{-1}$) on the red side. The

DBSP spectra were reduced using the `dbsp_drp` pipeline (Roberson et al. 2022), which is based on `PyPeIt` (Prochaska et al. 2020).

The ESI observation was performed in the Echellette mode with a 0''.75 wide slit, which gives a resolving power of $R = 5350$ (i.e., $\sigma_{\text{inst}} = 24 \text{ km s}^{-1}$). The ESI spectrum was reduced using the `MAKEE` pipeline following standard procedures. Flux calibration was not performed. We normalized the spectra by fitting third-order cubic splines to the continuum, with prominent emission and absorption lines masked.

Observations with DeVeny were performed with the 300/4000 grating, with a grating tilt angle of 23°.13 to yield a central wavelength of 5800 Å, the clear rear filter, and a slit width of 1''.5. This gives $\sigma_{\text{inst}} \approx 169 \text{ km s}^{-1}$. DeVeny spectra were reduced with `PyRAF`, including bias correction and flat-fielding.

Table 12
Log of AT2021ehb Optical Spectroscopy

Start Date	δt (days)	Telescope	Instrument	Wavelength Range (Å)	Slit Width (")	Exp. (s)
2021-03-25.1	-22	P60	SEDM	3770–9223	...	2160
2021-03-27.1	-20	P60	SEDM	3770–9223	...	2160
2021-07-06.6	+79	Keck I	LRIS	3200–10250	1.0	300
2021-08-01.4	+104	P200	DBSP	3410–5550, 5750–9995	1.5	900
2021-08-13.6	+116	Keck I	LRIS	3200–10250	1.0	300
2021-09-07.6	+141	Keck I	LRIS	3200–10250	1.0	300
2021-09-17.4	+150	P60	SEDM	3770–9223	...	2700
2021-10-27.5	+190	LDT	DeVeny	35868034	1.5	2400
2021-11-13.3	+206	P60	SEDM	3770–9223	...	2700
2021-12-03.3	+226	P60	SEDM	3770–9223	...	2700
2021-12-28.4	+250	Keck II	ESI	4000–10250	0.75	300
2022-01-05.2	+258	P60	SEDM	3770–9223	...	2700
2022-01-12.2	+265	P200	DBSP	3410–5550, 5750–9995	2.0	600
2022-01-20.3	+273	P60	SEDM	3770–9223	...	2700
2022-01-27.3	+280	P60	SEDM	3770–9223	...	2700
2022-02-06.3	+290	Keck I	LRIS	3200–10250	1.0	300
2022-03-27.1	+338	P200	DBSP	3410–5550, 5750–9995	1.5	1200

Note. The spectra are available on the TNS page of this source (<https://www.wis-tns.org/object/2021ehb>).

ORCID iDs

Yuhan Yao  <https://orcid.org/0000-0001-6747-8509>
 Wenbin Lu  <https://orcid.org/0000-0002-1568-7461>
 Muryel Guolo  <https://orcid.org/0000-0002-5063-0751>
 Dheeraj R. Pasham  <https://orcid.org/0000-0003-1386-7861>
 Suvi Gezari  <https://orcid.org/0000-0003-3703-5154>
 Keith C. Gendreau  <https://orcid.org/0000-0001-7115-2819>
 Fiona Harrison  <https://orcid.org/0000-0003-2992-8024>
 S. Bradley Cenko  <https://orcid.org/0000-0003-1673-970X>
 S. R. Kulkarni  <https://orcid.org/0000-0001-5390-8563>
 Jon M. Miller  <https://orcid.org/0000-0003-2869-7682>
 Dominic J. Walton  <https://orcid.org/0000-0001-5819-3552>
 Javier A. García  <https://orcid.org/0000-0003-3828-2448>
 Sjoert van Velzen  <https://orcid.org/0000-0002-3859-8074>
 Kate D. Alexander  <https://orcid.org/0000-0002-8297-2473>
 James C. A. Miller-Jones  <https://orcid.org/0000-0003-3124-2814>
 Matt Nicholl  <https://orcid.org/0000-0002-2555-3192>
 Erica Hammerstein  <https://orcid.org/0000-0002-5698-8703>
 Pavel Medvedev  <https://orcid.org/0000-0002-9380-8708>
 Daniel Stern  <https://orcid.org/0000-0003-2686-9241>
 Vikram Ravi  <https://orcid.org/0000-0002-7252-5485>
 Joshua S. Bloom  <https://orcid.org/0000-0002-7777-216X>
 Matthew J. Graham  <https://orcid.org/0000-0002-3168-0139>
 Erik C. Kool  <https://orcid.org/0000-0002-7252-3877>
 Ashish A. Mahabal  <https://orcid.org/0000-0003-2242-0244>
 Frank J. Masci  <https://orcid.org/0000-0002-8532-9395>
 Josiah Purdum  <https://orcid.org/0000-0003-1227-3738>
 Ben Rusholme  <https://orcid.org/0000-0001-7648-4142>
 Yashvi Sharma  <https://orcid.org/0000-0003-4531-1745>
 Roger Smith  <https://orcid.org/0000-0001-7062-9726>
 Jesper Sollerman  <https://orcid.org/0000-0003-1546-6615>

References

- Alam, S., Albareti, F. D., Allende Prieto, C., et al. 2015, *ApJS*, **219**, 12
 Alexander, K. D., Berger, E., Guillochon, J., Zauderer, B. A., & Williams, P. K. G. 2016, *ApJL*, **819**, L25
 Alexander, K. D., Goodwin, A. J., Miller-Jones, J., et al. 2021, *TNSAN*, **309**, 1
 Alexander, K. D., van Velzen, S., Horesh, A., & Zauderer, B. A. 2020, *SSRv*, **216**, 81
 Anders, E., & Grevesse, N. 1989, *GeCoA*, **53**, 197
 Andreoni, I., Coughlin, M., Ahumada, T., et al. 2022, *GCN*, **31590**, 1
 Arnaud, K. A. 1996, in *ASP Conf. Ser. 101, Astronomical Data Analysis Software and Systems V*, ed. V. Systems, G. H. Jacoby, & J. Barnes (San Francisco, CA: ASP), 17
 Astropy Collaboration, Robitaille, T. P., Tollerud, E. J., et al. 2013, *A&A*, **558**, A33
 Auchettl, K., Guillochon, J., & Ramirez-Ruiz, E. 2017, *ApJ*, **838**, 149
 Auchettl, K., Ramirez-Ruiz, E., & Guillochon, J. 2018, *ApJ*, **852**, 37
 Balbus, S. A., & Hawley, J. F. 1991, *ApJ*, **376**, 214
 Baldassare, V. F., Dickey, C., Geha, M., & Reines, A. E. 2020, *ApJL*, **898**, L3
 Bellm, E. C., Kulkarni, S. R., Graham, M. J., et al. 2019, *PASP*, **131**, 018002
 Blagorodnova, N., Gezari, S., Hung, T., et al. 2017, *ApJ*, **844**, 46
 Blagorodnova, N., Neill, J. D., Walters, R., et al. 2018, *PASP*, **130**, 035003
 Blanchard, P. K., Nicholl, M., Berger, E., et al. 2017, *ApJ*, **843**, 106
 Bloom, J. S., Giannios, D., Metzger, B. D., et al. 2011, *Sci*, **333**, 203
 Bonnerot, C., Lu, W., & Hopkins, P. F. 2021, *MNRAS*, **504**, 4885
 Brightman, M., Ward, C., Stern, D., et al. 2021, *ApJ*, **909**, 102
 Brown, G. C., Levan, A. J., Stanway, E. R., et al. 2015, *MNRAS*, **452**, 4297
 Burrows, D. N., Hill, J. E., Nousek, J. A., et al. 2005, *SSRv*, **120**, 165
 Burrows, D. N., Kennea, J. A., Ghisellini, G., et al. 2011, *Natur*, **476**, 421
 Cappellari, M. 2017, *MNRAS*, **466**, 798
 Cappellari, M., & Emsellem, E. 2004, *PASP*, **116**, 138
 Cardelli, J. A., Clayton, G. C., & Mathis, J. S. 1989, *ApJ*, **345**, 245
 Cash, W. 1979, *ApJ*, **228**, 939
 Cendes, Y., Alexander, K. D., Berger, E., et al. 2021a, *ApJ*, **919**, 127
 Cendes, Y., Eftekhari, T., Berger, E., & Polisensky, E. 2021b, *ApJ*, **908**, 125
 Cendes, Y., Berger, E., Alexander, K., et al. 2022, arXiv:2206.14297
 Cenko, B. 2022, *GCN*, **31500**, 1
 Cenko, S. B., Fox, D. B., Moon, D.-S., et al. 2006, *PASP*, **118**, 1396
 Cenko, S. B., Krimm, H. A., Horesh, A., et al. 2012, *ApJ*, **753**, 77
 Conroy, C., Gunn, J. E., & White, M. 2009, *ApJ*, **699**, 486
 Cutri, R. M., Wright, E. L., Conrow, T., et al. 2014, *yCat*, **2328**, 0
 Dai, L., McKinney, J. C., & Miller, M. C. 2015, *ApJL*, **812**, L39
 Dai, L., McKinney, J. C., Roth, N., Ramirez-Ruiz, E., & Miller, M. C. 2018, *ApJL*, **859**, L20
 Dauser, T., Garcia, J., Parker, M. L., Fabian, A. C., & Wilms, J. 2014, *MNRAS*, **444**, L100
 Dauser, T., Garcia, J., Walton, D. J., et al. 2016, *A&A*, **590**, A76
 Davis, S. W., & El-Abd, S. 2019, *ApJ*, **874**, 23
 Dekany, R., Smith, R. M., Riddle, R., et al. 2020, *PASP*, **132**, 038001
 Done, C., Gierliński, M., & Kubota, A. 2007, *A&ARv*, **15**, 1
 Donley, J. L., Brandt, W. N., Eracleous, M., & Boller, T. 2002, *AJ*, **124**, 1308
 Eftekhari, T., Berger, E., Zauderer, B. A., Margutti, R., & Alexander, K. D. 2018, *ApJ*, **854**, 86
 Evans, P. A., Beardmore, A. P., Page, K. L., et al. 2009, *MNRAS*, **397**, 1177
 Ezhikode, S. H., Dewangan, G. C., Misra, R., & Philip, N. S. 2020, *MNRAS*, **495**, 3373
 Falcke, H., Körding, E., & Markoff, S. 2004, *A&A*, **414**, 895
 Fender, R. P., Belloni, T. M., & Gallo, E. 2004, *MNRAS*, **355**, 1105
 Ferrarese, L., & Ford, H. 2005, *SSRv*, **116**, 523
 Flewelling, H. A., Magnier, E. A., Chambers, K. C., et al. 2020, *ApJS*, **251**, 7
 Foreman-Mackey, D., Hogg, D. W., Lang, D., & Goodman, J. 2013, *PASP*, **125**, 306
 Foreman-Mackey, D., Sick, J., & Johnson, B. 2014, python-fsps: Python bindings to FSPP (v0.1.1), v0.1.1, Zenodo, doi:10.5281/zenodo.12157
 Fremling, C., Graham, M., Kulkarni, S., & Kasliwal, M. 2021, *TNSAN*, **318**, 1
 Fremling, C., Sollerman, J., Taddia, F., et al. 2016, *A&A*, **593**, A68
 French, K. D., Wevers, T., Law-Smith, J., Graur, O., & Zabludoff, A. I. 2020, *SSRv*, **216**, 32
 Gabriel, C., Denby, M., Fyfe, D. J., et al. 2004, in *ASP Conf. Ser. 314, Astronomical Data Analysis Software and Systems (ADASS) XIII*, ed. F. Ochsenbein, M. G. Allen, & D. Egret (San Francisco, CA: ASP), 759
 García, J., Dauser, T., Lohfink, A., et al. 2014, *ApJ*, **782**, 76
 Gendreau, K. C., Arzoumanian, Z., Adkins, P. W., et al. 2016, *Proc. SPIE*, **9905**, 99051H
 Gezari, S. 2021, *ARA&A*, **59**, 21
 Gezari, S., Cenko, S. B., & Arcavi, I. 2017, *ApJL*, **851**, L47
 Gezari, S., Hammerstein, E., Yao, Y., et al. 2021, *TNSAN*, **103**, 1
 Goodwin, A. J., van Velzen, S., Miller-Jones, J. C. A., et al. 2022, *MNRAS*, **511**, 5328
 Graham, M. J., Kulkarni, S. R., Bellm, E. C., et al. 2019, *PASP*, **131**, 078001
 Greene, J. E., Strader, J., & Ho, L. C. 2020, *ARA&A*, **58**, 257
 Gültekin, K., King, A. L., Cackett, E. M., et al. 2019, *ApJ*, **871**, 80
 Guolo, M., Ruschel-Dutra, D., Grupe, D., et al. 2021, *MNRAS*, **508**, 144
 Hammerstein, E., van Velzen, S., Gezari, S., et al. 2022, arXiv:2203.01461
 Harrison, F. A., Craig, W. W., Christensen, F. E., et al. 2013, *ApJ*, **770**, 103
 Heasarc 2014, HEASoft: Unified Release of FTOOLS and XANADU, Astrophysics Source Code Library, ascl:1408.004
 HI4PI Collaboration, Ben Bekhti, N., Flöer, L., et al. 2016, *A&A*, **594**, A116
 Hinkle, J. T., Holoien, T. W.-S., Auchettl, K., et al. 2021, *MNRAS*, **500**, 1673
 Horesh, A., Cenko, S. B., & Arcavi, I. 2021a, *NatAs*, **5**, 491
 Horesh, A., Sfaradi, I., Fender, R., et al. 2021b, *ApJL*, **920**, L5
 Hunter, J. D. 2007, *CSE*, **9**, 90
 Jiang, Y.-F., Guillochon, J., & Loeb, A. 2016, *ApJ*, **830**, 125
 Johnson, B. D., Leja, J., Conroy, C., & Speagle, J. S. 2021, *ApJS*, **254**, 22
 Kaastra, J. S., & Bleeker, J. A. M. 2016, *A&A*, **587**, A151
 Kajava, J. J. E., Giustini, M., Saxton, R. D., & Miniutti, G. 2020, *A&A*, **639**, A100
 Kallman, T., & Bautista, M. 2001, *ApJS*, **133**, 221
 Kara, E., Dai, L., Reynolds, C. S., & Kallman, T. 2018, *MNRAS*, **474**, 3593
 Kara, E., Miller, J. M., Reynolds, C., & Dai, L. 2016, *Natur*, **535**, 388
 Kellogg, E., Baldwin, J. R., & Koch, D. 1975, *ApJ*, **199**, 299
 Kormendy, J., & Ho, L. C. 2013, *ARA&A*, **51**, 511
 Law, N. M., Kulkarni, S. R., Dekany, R. G., et al. 2009, *PASP*, **121**, 1395
 Leloudas, G., Dai, L., Arcavi, I., et al. 2019, *ApJ*, **887**, 218
 Lightman, A. P., & Eardley, D. M. 1974, *ApJL*, **187**, L1
 Lu, W., & Bonnerot, C. 2020, *MNRAS*, **492**, 686
 Lu, W., & Kumar, P. 2018, *ApJ*, **865**, 128
 Ludlam, R. M., Cackett, E. M., García, J. A., et al. 2022, *ApJ*, **927**, 112
 Madsen, K. K., Beardmore, A. P., Forster, K., et al. 2017, *AJ*, **153**, 2

- Martin, D. C., Fanson, J., Schiminovich, D., et al. 2005, *ApJL*, 619, L1
- Masci, F. J., Laher, R. R., Rusholme, B., et al. 2019, *PASP*, 131, 018003
- McHardy, I. M., Koerding, E., Knigge, C., Uttley, P., & Fender, R. P. 2006, *Natur*, 444, 730
- McMullin, J. P., Waters, B., Schiebel, D., Young, W., & Golap, K. 2007, in ASP Conf. Ser. 376, *Astronomical Data Analysis Software and Systems XVI*, ed. R. A. Shaw, F. Hill, & D. J. Bell (San Francisco, CA: ASP), 127
- Merloni, A., Heinz, S., & Di Matteo, T. 2003, *MNRAS*, 345, 1057
- Metzger, B. D., & Stone, N. C. 2016, *MNRAS*, 461, 948
- Middleton, M. J., Miller-Jones, J. C. A., Markoff, S., et al. 2013, *Natur*, 493, 187
- Miller, J. M., Reynolds, M. T., Yun, S. B., et al. 2022a, *ATel*, 15179, 1
- Miller, J. M., Reynolds, M. T., Zoghbi, A., et al. 2022b, *ATel*, 15205, 1
- Miller, K. A., & Stone, J. M. 2000, *ApJ*, 534, 398
- Miller, M. C. 2015, *ApJ*, 805, 83
- Mitsuda, K., Inoue, H., Koyama, K., et al. 1984, *PASJ*, 36, 741
- Munoz-Darias, T., Coriat, M., Plant, D. S., et al. 2013, *MNRAS*, 432, 1330
- Mummery, A., & Balbus, S. A. 2020, *MNRAS*, 492, 5655
- Munoz-Arancibia, A., Forster, F., Bauer, F. E., et al. 2021, *Transient Name Server Discovery Report* 651
- Narayan, R., & Quataert, E. 2005, *Sci*, 307, 77
- Nicholl, M., Lanning, D., Ramsden, P., et al. 2022, *MNRAS*, 515, 5604
- Nicholl, M., Wevers, T., Oates, S. R., et al. 2020, *MNRAS*, 499, 482
- Nordin, J., Brinnet, V., van Santen, J., et al. 2019, *A&A*, 631, A147
- Oke, J. B., & Gunn, J. E. 1982, *PASP*, 94, 586
- Oke, J. B., Cohen, J. G., Carr, M., et al. 1995, *PASP*, 107, 375
- Parkinson, E. J., Knigge, C., Matthews, J. H., et al. 2022, *MNRAS*, 510, 5426
- Pasham, D., Yao, Y., Gendreau, K., et al. 2022, *ATel*, 15232, 1
- Pasham, D. R., Cenko, S. B., Sadowski, A., et al. 2017, *ApJL*, 837, L30
- Pasham, D. R., Cenko, S. B., Levan, A. J., et al. 2015, *ApJ*, 805, 68
- Perley, D. A. 2019, *PASP*, 131, 084503
- Perley, R. A., Chandler, C. J., Butler, B. J., & Wrobel, J. M. 2011, *ApJL*, 739, L1
- Piran, T., Svirski, G., Krolik, J., Cheng, R. M., & Shiokawa, H. 2015, *ApJ*, 806, 164
- Predehl, P., Andritschke, R., Arefiev, V., et al. 2021, *A&A*, 647, A1
- Prochaska, J., Hennawi, J., Westfall, K., et al. 2020, *JOSS*, 5, 2308
- Prugniel, P., & Soubiran, C. 2001, *A&A*, 369, 1048
- Prugniel, P., Soubiran, C., Koleva, M., & Le Borgne, D. 2007, *arXiv:astro-ph/0703658*
- Raftery, A. E. 1995, *Sociol. Methodol.*, 25, 111
- Rau, A., Kulkarni, S. R., Law, N. M., et al. 2009, *PASP*, 121, 1334
- Rees, M. J. 1988, *Natur*, 333, 523
- Reeves, J., Done, C., Pounds, K., et al. 2008, *MNRAS Lett.*, 385, L108
- Remillard, R. A., & McClintock, J. E. 2006, *ARA&A*, 44, 49
- Remillard, R. A., Loewenstein, M., Steiner, J. F., et al. 2022, *AJ*, 163, 130
- Reynolds, C. S., Brenneman, L. W., Lohfink, A. M., et al. 2012, *ApJ*, 755, 88
- Rigault, M., Neill, J. D., Blagorodnova, N., et al. 2019, *A&A*, 627, A115
- Roberson, M., Fremling, C., & Kasliwal, M. 2022, *JOSS*, 7, 3612
- Roming, P. W. A., Kennedy, T. E., Mason, K. O., et al. 2005, *SSRv*, 120, 95
- Rosswog, S., Ramirez-Ruiz, E., & Hix, W. R. 2009, *ApJ*, 695, 404
- Roth, N., Kasen, D., Guillochon, J., & Ramirez-Ruiz, E. 2016, *ApJ*, 827, 3
- Ruan, J. J., Anderson, S. F., Eraclous, M., et al. 2019, *ApJ*, 883, 76
- Saxton, R., Komossa, S., Auchettl, K., & Jonker, P. G. 2020, *SSRv*, 216, 85
- Sazonov, S., Gilfanov, M., Medvedev, P., et al. 2021, *MNRAS*, 508, 3820
- Schlafly, E. F., & Finkbeiner, D. P. 2011, *ApJ*, 737, 103
- Sfaradi, I., Horesh, A., Fender, R., et al. 2022, *ApJ*, 933, 176
- Shakura, N. I., & Sunyaev, R. A. 1973, *A&A*, 24, 337
- Shakura, N. I., & Sunyaev, R. A. 1976, *MNRAS*, 175, 613
- Shappee, B. J., Prieto, J. L., Grupe, D., et al. 2014, *ApJ*, 788, 48
- Sheinis, A. I., Bolte, M., Epps, H. W., et al. 2002, *PASP*, 114, 851
- Shen, R.-F., & Matzner, C. D. 2014, *ApJ*, 784, 87
- Shimura, T., & Takahara, F. 1995, *ApJ*, 445, 780
- Shu, X., Zhang, W., Li, S., et al. 2020, *NatCo*, 11, 5876
- Skrutskie, M. F., Cutri, R. M., Stiening, R., et al. 2006, *AJ*, 131, 1163
- Steele, I. A., Smith, R. J., Rees, P. C., et al. 2004, *Proc. SPIE*, 5489, 679
- Stein, R., Velzen, S. v., Kowalski, M., et al. 2021, *NatAs*, 5, 510
- Steiner, J. F., Narayan, R., McClintock, J. E., & Ebisawa, K. 2009, *PASP*, 121, 1279
- Strubbe, L. E., & Quataert, E. 2009, *MNRAS*, 400, 2070
- Strüder, L., Briel, U., Dennerl, K., et al. 2001, *A&A*, 365, L18
- Sunyaev, R., Arefiev, V., Babyshkin, V., et al. 2021, *A&A*, 656, A132
- Tananbaum, H., Avni, Y., Branduardi, G., et al. 1979, *ApJL*, 234, L9
- Techevskoy, A., Metzger, B. D., Giannios, D., & Kelley, L. Z. 2014, *MNRAS*, 437, 2744
- Tetarenko, A. J., Sivakoff, G. R., Miller-Jones, J. C. A., et al. 2017, *MNRAS*, 469, 3141
- Tetarenko, A. J., Sivakoff, G. R., Miller-Jones, J. C. A., et al. 2019, *MNRAS*, 482, 2950
- Tetarenko, B. E., Sivakoff, G. R., Heinke, C. O., & Gladstone, J. C. 2016, *ApJS*, 222, 15
- Thomsen, L. L., Kwan, T., Dai, L., Wu, S., & Ramirez-Ruiz, E. 2022, *arXiv:2206.02804*
- Thomsen, L. L., Lixin Dai, J., Ramirez-Ruiz, E., Kara, E., & Reynolds, C. 2019, *ApJL*, 884, L21
- Tonry, J. L., Denneau, L., Heinze, A. N., et al. 2018, *PASP*, 130, 064505
- Ulmer, A. 1999, *ApJ*, 514, 180
- van Velzen, S., Gezari, S., Cenko, S. B., et al. 2019, *ApJ*, 872, 198
- van Velzen, S., Gezari, S., Hammerstein, E., et al. 2021, *ApJ*, 908, 4
- Verner, D. A., Ferland, G. J., Korista, K. T., & Yakovlev, D. G. 1996, *ApJ*, 465, 487
- Virtanen, P., Gommers, R., Oliphant, T. E., et al. 2020, *NatMe*, 17, 261
- Walton, D. J., Nardini, E., Fabian, A. C., Gallo, L. C., & Reis, R. C. 2013, *MNRAS*, 428, 2901
- Walton, D. J., Reis, R. C., Cackett, E. M., Fabian, A. C., & Miller, J. M. 2012, *MNRAS*, 422, 2510
- Walton, D. J., Alston, W. N., Kosec, P., et al. 2020, *MNRAS*, 499, 1480
- Waters, C. Z., Magnier, E. A., Price, P. A., et al. 2020, *ApJS*, 251, 4
- Wevers, T. 2020, *MNRAS Lett.*, 497, L1
- Wevers, T., van Velzen, S., Jonker, P. G., et al. 2017, *MNRAS*, 471, 1694
- Wevers, T., Pasham, D. R., van Velzen, S., et al. 2019a, *MNRAS*, 488, 4816
- Wevers, T., Stone, N. C., van Velzen, S., et al. 2019b, *MNRAS*, 487, 4136
- Wevers, T., Pasham, D. R., van Velzen, S., et al. 2021, *ApJ*, 912, 151
- Williams, P. K. G., Clavel, M., Newton, E., & Rzhzhkov, D. 2017, *pkwit: Astronomical utilities in Python, Astrophysics Source Code Library, ascl:1704.001*
- Wilms, J., Allen, A., & McCray, R. 2000, *ApJ*, 542, 914
- Yao, Y. 2021, *Transient Name Server Classification Report* 2295, 1
- Yao, Y., Brightman, M., Gezari, S., et al. 2021, *TNSAN*, 183, 1
- Yao, Y., Pasham, D. R., & Gendreau, K. C. 2022a, *ATel*, 15230, 1
- Yao, Y., Pasham, D. R., Gendreau, K. C., et al. 2022b, *ATel*, 15217, 1
- Yao, Y., Miller, A. A., Kulkarni, S. R., et al. 2019, *ApJ*, 886, 152
- Yao, Y., De, K., Kasliwal, M. M., et al. 2020, *ApJ*, 900, 46
- Yuan, F., Cui, W., & Narayan, R. 2005, *ApJ*, 620, 905
- Yuan, F., & Narayan, R. 2014, *ARA&A*, 52, 529
- Zauderer, B. A., Berger, E., Margutti, R., et al. 2013, *ApJ*, 767, 152
- Zauderer, B. A., Berger, E., Soderberg, A. M., et al. 2011, *Natur*, 476, 425